

## Seismology on Mars: An analysis of direct, reflected, and converted seismic body waves with implications for interior structure

C. Durán <sup>a,\*</sup>, A. Khan <sup>a,b</sup>, S. Ceylan <sup>a</sup>, G. Zenhäusern <sup>a</sup>, S. Stähler <sup>a</sup>, J.F. Clinton <sup>a,c</sup>, D. Giardini <sup>a</sup>

<sup>a</sup> Institute of Geophysics, ETH Zurich, Zurich, Switzerland

<sup>b</sup> Physik-Institut, University of Zurich, Zurich, Switzerland

<sup>c</sup> Swiss Seismological Service, ETH Zurich, Zurich, Switzerland



### ARTICLE INFO

#### Keywords:

Marsquakes  
Mars' interior structure  
Seismic phases  
Body waves  
Receiver functions  
Inversion

### ABSTRACT

The InSight (Interior Exploration using Seismic Investigations, Geodesy and Heat Transport) mission has been collecting high-quality seismic data on Mars since early 2019 that provide the first direct observations of its interior structure. Here we report on a complete analysis of the part of the marsquakes known as the low-frequency seismic events (main energy below 1 Hz) that are sensitive to the deep interior. To identify body-wave arrivals in the highly-scattered martian seismograms, we employ four complementary approaches: 1) time-domain envelopes; 2) polarised waveforms and their time-domain envelopes; 3) polarisation analysis; and 4) waveform matching. Through careful application of this processing scheme to each marsquake, we are able to significantly increase the number of phase picks relative to earlier analyses (from 41 to 76), including body-wave arrivals from direct (P and S), reflected (PP, SS, PPP, SSS, and ScS), and converted (Ps and Sp) phases. To constrain the depth of the marsquakes, we also identify depth phases (pP and sS). Following this, we invert an initial set of phase picks for models of interior structure, event distance, and depth, while predicting travel times for seismic phases not identified at the outset. Based on the predictions, we repick (every pick is subject to our processing scheme), thereby enlarging our differential travel-time data set (all picks are relative to the main P-wave arrival), and subsequently re-invert for an updated set of interior structure models, distances, and depths. Proceeding thus, we present updated radial seismic velocity models of the crust, mantle, and core. We observe crustal interfaces at average depths of 10, 25, and 45 km, respectively, of which the former two are interpreted as intra-crustal interfaces and the latter as the crust-mantle boundary. We find an upper mantle structure consistent with a low-velocity zone associated with a thermal lithosphere and a thermal gradient in the range 2.4–2.9 K/km that extends to a depth of ~450 km. The thermal structure of the Martian mantle indicates potential and core-mantle-boundary temperatures in the ranges 1650–1750 K and 1900–2100 K, respectively, implying an entirely liquid core at present. Based on the identification of ScS phases, we obtain an improved estimate of the Martian core radius (1820–1870 km) and mean core density (6–6.2 g/cm<sup>3</sup>).

### 1. Introduction

Extraterrestrial seismology saw its advent with the Apollo program and the installation of seismometers on the lunar surface (Latham et al., 1970). Seismic investigations continued on Mars as part of the Viking missions, but were mainly curtailed by mission restrictions that limited the seismometer to the lander. As a consequence, the Viking seismic recordings were dominated by wind-induced noise related to the shaking of the lander (Anderson et al., 1977). The Venera 13 and 14 landers also carried seismometers to the surface of Venus, but, because of environmental conditions, the instrument only operated for a short

duration (~1 h) during which no venusquakes were recorded (Ksanfomaliti et al., 1982).

With the arrival of InSight (Interior Exploration using Seismic Investigations, Geodesy and Heat Transport) on Mars and the deployment of SEIS (Seismic Experiment for Interior Structure) on its surface, Mars represents the second extra-terrestrial body for which we have seismic data (Banerdt et al., 2020). The successful detection of marsquakes and acquisition of high-quality seismic data since early 2019 (Lognonné et al., 2020; Giardini et al., 2020) have proven a major milestone in planetary seismology. It has allowed us to obtain the first close-up view of the crust, mantle, and core of Mars (Knapmeyer-Endrun et al., 2021;

\* Corresponding author.

E-mail address: [cecilia.duran@erdw.ethz.ch](mailto:cecilia.duran@erdw.ethz.ch) (C. Durán).

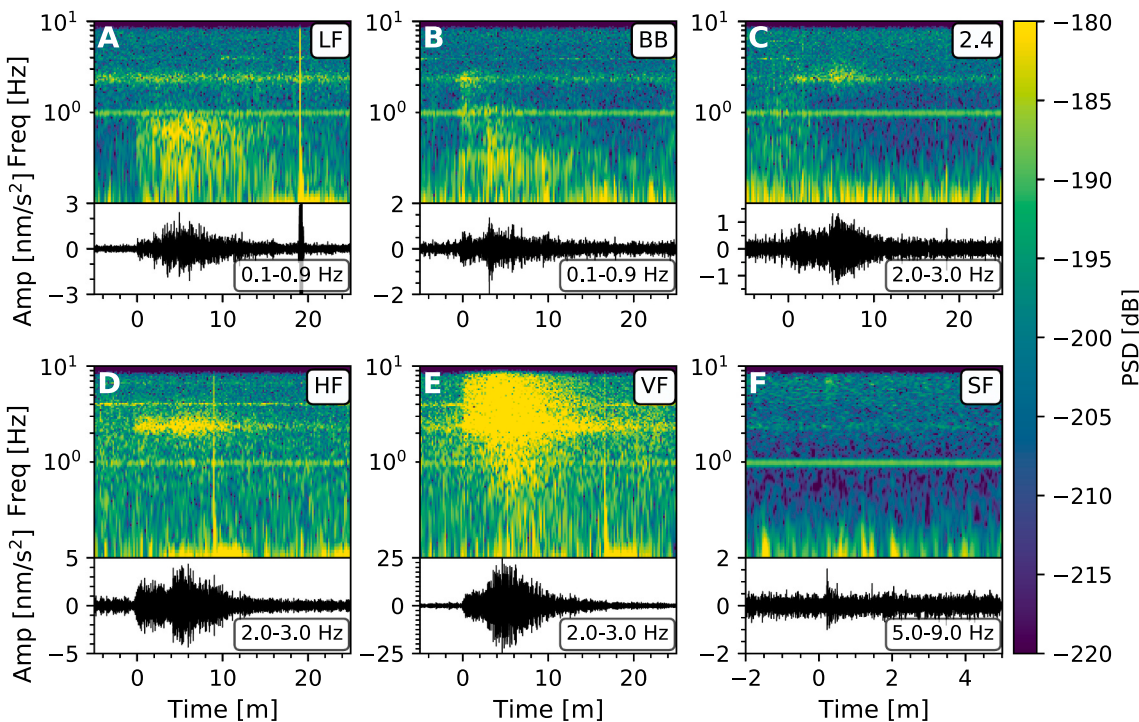


**Fig. 1.** Vertical-component spectrograms (top panels of each plot) and filtered waveforms (bottom panels of each plot) for the main seismic event types detected on Mars. Marsquakes shown include the low-frequency (LF) event S0809a (A), broad-band (BB) event S0784a (B), 2.4-Hz event S0477a (C), high-frequency event (HF) S0331a (D), very high-frequency (VF) event S0794a (E), and super high-frequency (SF) event T0190a (F). Events are labelled by mission Sol (S for LF, BB, 2.4-Hz, HF, and VF events and T for SF events) of occurrence and sub-labelled alphabetically for Sols with more than one event.

Khan et al., 2021; Stähler et al., 2021).

Unlike the Apollo lunar seismic array, which consisted of 4 concomitantly-working seismic stations (Nakamura, 1983; Lognonné and Johnson, 2007; Khan et al., 2013; Garcia et al., 2019), locating marsquakes with a single station is challenging (Böse et al., 2017), particularly in view of the fact that interior structure needs to be determined simultaneously (Panning et al., 2015; Khan et al., 2016; Drilleau et al., 2020). As discussed in the aforementioned studies and shown on the basis of Martian seismic data (Giardini et al., 2020), the distance to a marsquake can be determined from observations of P- and S-wave arrivals and an a priori seismic model data base (Clinton et al., 2021). To image the planet's interior structure, a primary goal of the InSight mission (Banerdt et al., 2020), requires moving beyond the identification of the main P- and S-wave arrivals; yet, identifying secondary arrivals (e.g., surface-reflections) has proved more difficult because marsquake waveforms are characterized by relatively strong scattering coda (Lognonné et al., 2020). Although less strong than the notorious coda that beset seismograms from the Moon, alternative and complimentary methods have had to be devised to enable picking secondary phase arrivals, including the use of narrow-band-filtered time-domain envelopes, polarisation filters and vespagrams, and waveform matching techniques (Khan et al., 2021). Polarisation filters, for example, enhance linearly polarised waves such as body waves and were used to detect core reflections in the Apollo seismic data (Weber et al., 2011).

The marsquake catalog (InSight Marsquake Service, 2021), which currently numbers more than 1000 events, classifies marsquakes into two main categories: low- and high-frequency, on account of their main frequency content. Low-frequency (LF) events are characterized by having energy dominantly below 1 Hz, whereas high-frequency (HF) events have energy dominantly above 1 Hz (Clinton et al., 2021; Giardini et al., 2020; van Driel et al., 2021). While HF events outnumber LF events, they are yet to be fully understood. As a consequence, we focus on the high-quality LF events recorded by InSight and provide a

complete and independent analysis of the entire LF event data set (Sols 0–922), including the direct and reflected body-wave arrivals reported on earlier (Khan et al., 2021; Stähler et al., 2021), in addition to the converted body waves that have been employed to investigate crustal structure (Knapmeyer-Endrun et al., 2021).

In what follows, we commence with a brief overview of the types of seismic events that have been recorded hitherto (section 2). Following this, we provide a summary overview of the joint marsquake location and interior-structure-determination-method (section 3) building upon the work of Khan et al. (2016). Since the analysis and picking of seismic phase arrivals represents the most important part of the present study, we detail the processing of the seismic data and the picking procedure (section 4). Armed with an initial set of phase picks (P, pP, PP, S, sS, SS, and ScS), we perform a preliminary inversion for distance, depth and interior structure, while predicting arrival times of other seismic phases (e.g., PPP, SSS, and PS) that are subsequently compared with the seismic data for the purpose of picking additional phases (section 5). This allows us to enlarge our initial set of phase picks, after which we perform another joint-location-interior-structure-inversion to update the initial results (sections 6 and 7).

The procedure works iteratively and seeks to continuously update location and model structure with information from the latest seismic events. Relative to the 8 LF events considered in Khan et al. (2021), we have expanded the number of usable LF events to 14. This represents a significant increase in disposable seismic arrival time picks (76 versus 41), which allows for improved imaging of the Martian interior. Finally, we briefly present and discuss the new velocity structure of Mars.

## 2. Brief overview of InSight seismic data

A geophysical package including a very broadband (VBB) and a short-period (SP) seismometer (SEIS) (for instrumental details see Lognonné et al. (2019)) was successfully delivered to the Martian surface by InSight on 26 November 2018. Under several layers of thermal

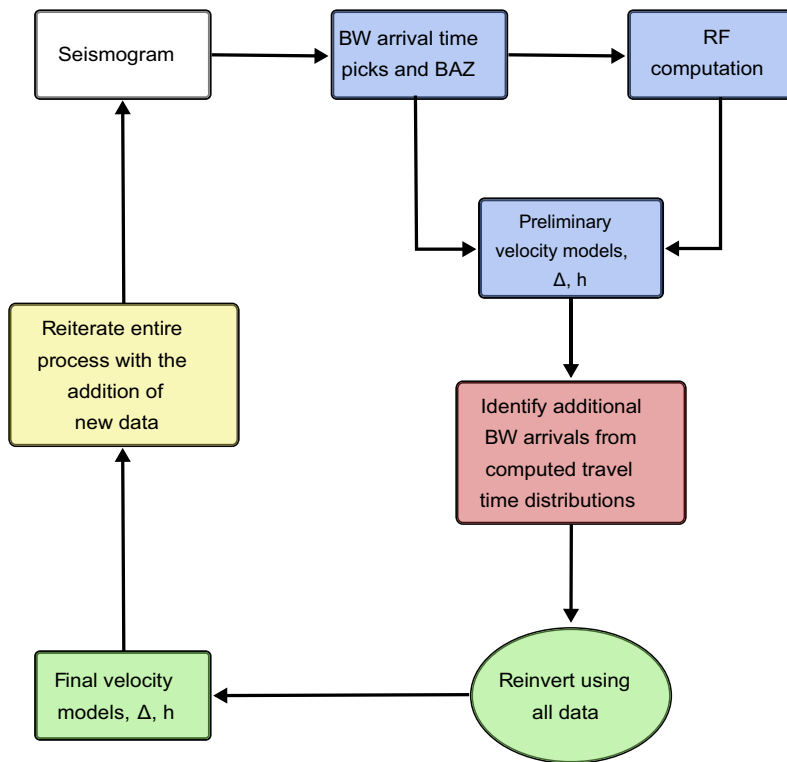


**Fig. 2.** Joint seismic event-location and structure-inversion scheme. The procedure is divided into four stages as described in section 3 and includes a data (martian seismograms) input stage (white box), followed by a data processing, seismic body wave picking, and preliminary inversion stage (blue boxes), after which we look for additional seismic phases (red box) and re-invert the expanded data set (green boxes). The entire process works iteratively with the addition of new events (yellow box). BW, BAZ, RF,  $\Delta$ , and  $h$  refer to body wave, back-azimuth, receiver function, epicentral distance, and source depth, respectively. (For interpretation of the references to colour in this figure legend, the reader is referred to the web version of this article.)

protection and very low self-noise, SEIS has recorded more than 1000 distinct events that have been identified and categorized into HF and LF events (Fig. 1) by the Marsquake Service (MQS) ([InSight Marsquake Service, 2021](#)).

The LF family (Fig. 1A-B) comprises events with energy mainly between 1 and 5 s. The events belonging to the LF family have an overall duration of  $\sim$ 10–30 min, and most of them show relatively clear P and S arrivals ([Clinton et al., 2021](#)). The LF family includes a subgroup of events that excites a mode at 2.4 Hz, which is a resonance most likely produced by a local subsurface feature ([Hobiger et al., 2021](#)), and are labelled as broadband (BB) events (Fig. 1B).

The HF events (Fig. 1C-D) contain energy above 1 Hz, generally reaching up to 12 Hz, with a duration ranging from 5 min to 20 min. The majority of these events are only visible within a very narrow frequency range of the 2.4 Hz ambient resonance. Both HF and LF events have comparable relative travel times of P and S arrivals, but the former are interpreted as marsquakes with propagation restricted to the crust, which acts as a waveguide ([Giardini et al., 2020](#); [van Driel et al., 2021](#)). Events in the HF family are further divided into three subgroups based on more detailed analysis of the spectral content: 2.4 Hz events (Fig. 1C) only excite the 2.4 Hz mode, and do not contain energy above 4 Hz; high frequency (HF) events (Fig. 1D) excite the 2.4 Hz mode and higher frequencies up to 10 Hz; and very high frequency (VF) events (Fig. 1E) strongly excite the horizontal components at frequencies above 5 Hz, reaching 10 Hz, and occasionally 35 Hz. An additional high-frequency signal that has been observed includes the super high frequency (SF) events (Fig. 1F) which, in contrast to most LF and HF events, have a duration of around 20 s and energy above 5 Hz and were interpreted as local thermal cracks ([Dahmen et al., 2021](#)).

Despite efforts to isolate the seismometer from atmospheric perturbations, SEIS is still highly sensitive to local weather conditions, and seasonal noise variation are present ([Ceylan et al., 2021](#)). During each sol, very large diurnal variations in noise are observed, limiting the detection of events mainly from the early evening hours until midnight, when the background Martian noise level is consistently low because of low wind speeds ([Banfield et al., 2020](#)). In general, the majority of the

observed events comprise small amplitude marsquakes that are difficult to resolve above the background ambient noise ([Giardini et al., 2020](#)). The InSight catalog (V.8 valid until October 1, 2021) consists of a total of 1286 seismic events, including 42 LF, 19 BB, 63 HF, 46 VF, 501 2.4 Hz, and 953 SF events. For the events for which epicentral distance has been estimated, magnitudes range between 1.1 and 3.7, with an uncertainty of  $\pm 0.4$  magnitude units based on incomplete knowledge of the focal mechanism and epicentral distance ([Clinton et al., 2021](#)). For the LF family of events, the moment magnitude is estimated by employing the spectral amplitude  $A_0$  and the epicentral distance  $\Delta$ , where  $A_0$  is determined from the square root of the long-period plateau of the power spectral density of the event displacement and  $\Delta$  is derived from travel-time alignment ([Böse et al., 2021](#)). For the HF family of events, a pair of magnitudes are computed based on the peak amplitude and the spectral fit of the 2.4 Hz resonance ([Böse et al., 2018, 2021](#)).

### 3. Joint marsquake location and interior structure determination

Our scheme for determining the location simultaneously with crust, mantle, and core structure is outlined in Fig. 2. The procedure consists of four main stages that work as follows.

*Input stage* (white box): Martian seismograms forms the input for our analysis.

*Stage 1* (blue boxes): The method relies on identifying direct (P and S), surface-reflected (PP and SS), core-reflected (ScS), and converted (Ps and Sp) body-wave arrivals to locate marsquakes in space (epicentral distance and back-azimuth). To determine the depth of the events we also look for depth phases (pP and sS). From observations of converted waves, we construct receiver functions (hereinafter RF) that are inverted jointly with body-wave arrivals in the form of differential travel times for a set of preliminary radial models of P- and S-wave speed, density, and source location.

*Stage 2* (red box): The preliminary models obtained in *stage 1* are employed to predict arrival times for other body-wave phases (e.g., PPP, SSS, etc.) that would otherwise escape positive identification because of

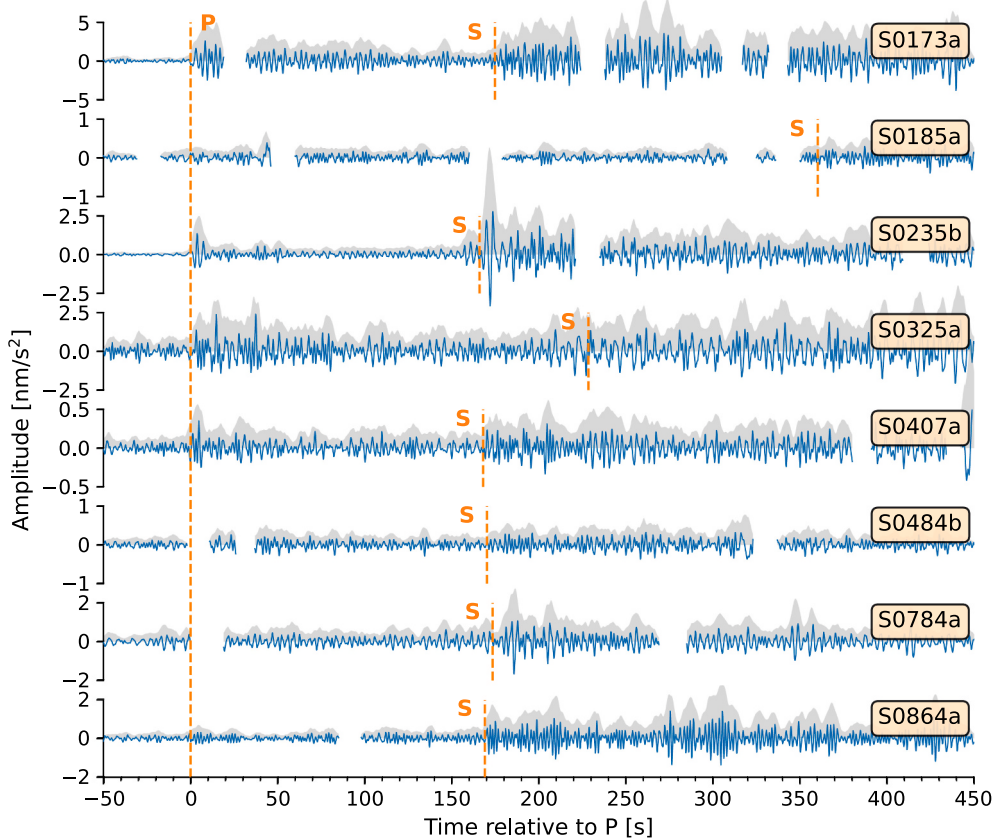


**Fig. 3.** Vertical-component broad-band filtered (1/8–1.4 Hz) seismograms for a series of low-frequency events (event labels are indicated in the yellow boxes) recorded by InSight. Waveforms are aligned using the direct P-wave arrival (labelled P, dashed line). S-wave arrivals are indicated by S. Time-domain envelopes are shown in grey. Waveforms are masked where glitches occurred to avoid misinterpretation of phases. (For interpretation of the references to colour in this figure legend, the reader is referred to the web version of this article.)

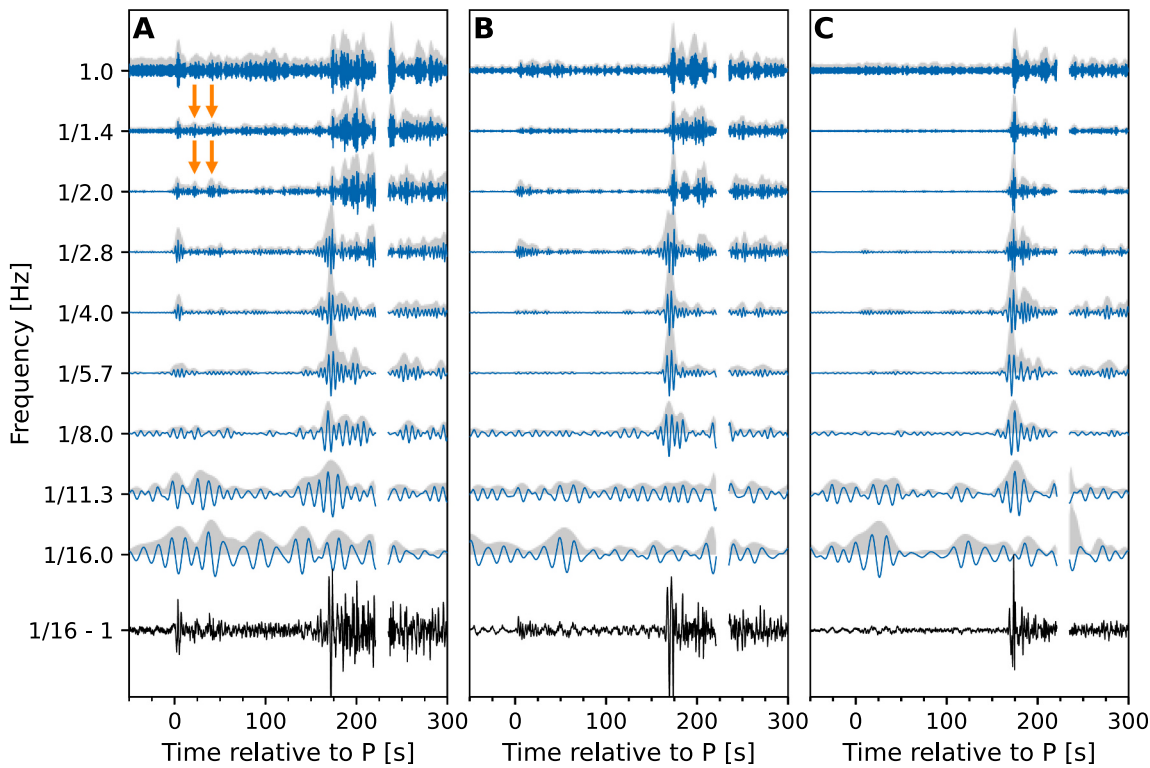


**Fig. 4.** Band-pass filtered (1/16–1 Hz) seismogram for event S0235b (bottom trace in black) and filtered waveforms and their envelopes across different frequency bands (filter banks) for (A) the vertical, (B) the radial, and (C) the transverse components. Filtered traces and their envelopes are shown in blue and grey, respectively. Waveforms are masked where glitches occurred to avoid misinterpretation of phases. Both traces and envelopes are normalized using their maximum amplitude. Vertically-downward pointing orange arrows point to potential surface-reflected P-wave arrivals. (For interpretation of the references to colour in this figure legend, the reader is referred to the web version of this article.)

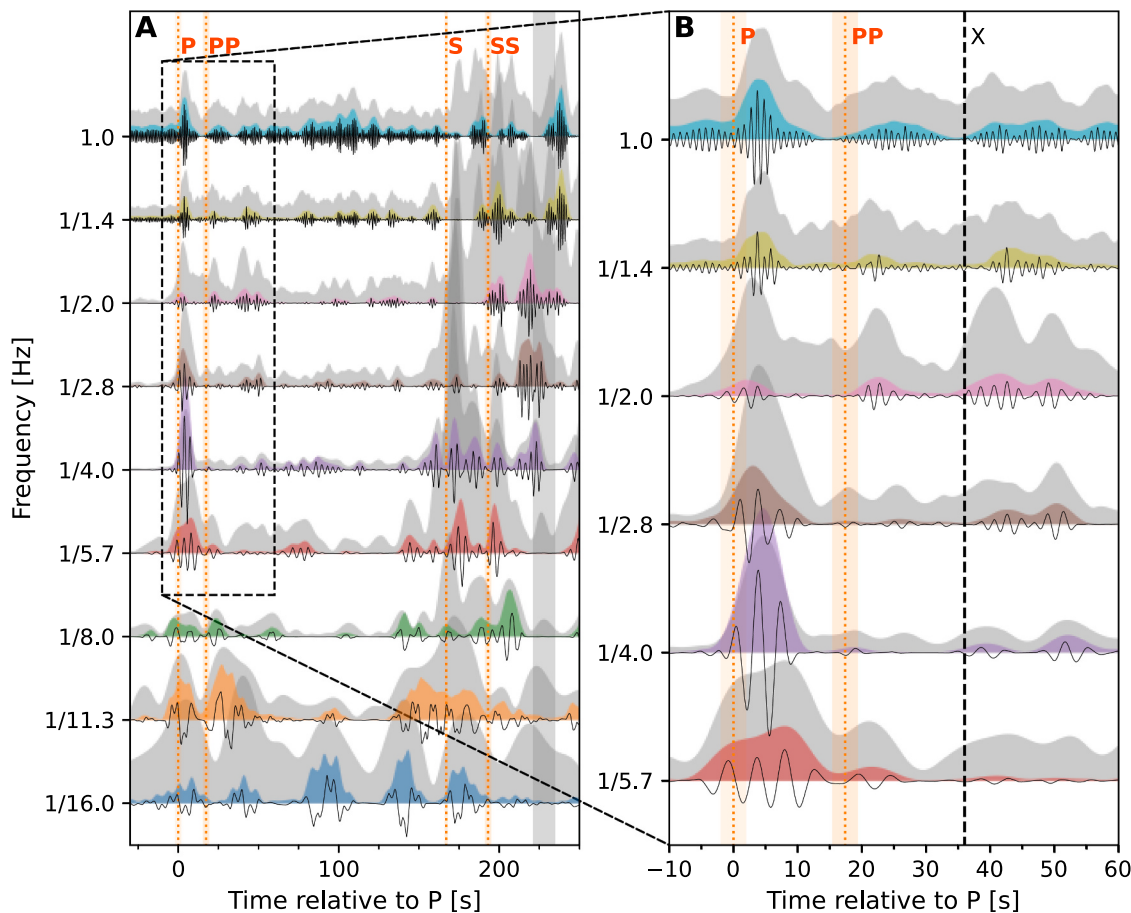


**Fig. 5.** Vertical-component time-domain envelopes and polarised traces for event S0235b across different frequency bands (filter banks). Grey envelopes depict unpolarised time-domain envelopes. Polarised traces and their envelopes are shown in black (lines) and colored envelopes, respectively. Initial seismic phase picks for S0235b are shown as vertical dotted lines. Orange bars indicate uncertainties on the arrival time picks. The vertical grey bar in panel (A) represents a glitch. Panel (B) shows a zoomed-in version of the P-wave phases in (A). The vertical dashed line in (B) denoted by X, indicates another possible seismic wave arrival. Amplitudes of traces and envelopes are normalized by their maxima and scaled for better visualisation.

low signal-to-noise ratio (SNR). For this purpose, we reanalyse the seismic data for the predicted phases using time-domain envelopes and polarised-filtered traces.

**Stage 3** (green boxes): With the identification of new body-wave arrivals in stage 2, we re-invert the expanded differential travel-time data set. Iterating thus improves location and model estimates.

**Stage 4** (yellow box): The entire procedure of updating previous models and event location is ensured through continued application of stages 1–3 to new event data.

#### 4. Data

In this section, we describe *stage 1* of our scheme, i. e., how the initial set of P, S, and reflected body-wave phases are picked, and how the receiver functions (RF) are processed. For this purpose, we employ the 14 highest-quality events from the LF family, labelled by mission Sol of occurrence and sub-labelled alphabetically for Sols with more than one event: S0167b, S0173a, S0183a, S0185a, S0235b, S0325a, S0407a, S0409d, S0484b, S0784a, S0802a, S0809a, S0820a, and S0864a. Each of these events is characterized by a high SNR and identifiable P- and S-wave arrivals. Estimation of back-azimuth is available for events: S0173a, S0183a, S0235b, S0784a, S0802a, S0820a, and S0864a from the polarisation analysis technique described in 4.1.3 and Clinton et al. (2021).

#### 4.1. Seismic phase identification: Direct and surface-reflected body waves

To identify body-wave phases, we employ four complementary approaches: 1) time-domain envelopes; 2) polarised waveforms and their time-domain envelopes; 3) polarisation analysis; and 4) waveform matching.

##### 4.1.1. Time-domain envelopes

Owing to the generally low SNR of Martian seismic events, most waveforms do not exhibit clear phase arrivals in the time-domain, with the exception of the direct P- and S-wave arrivals. This is illustrated in Fig. 3, which shows band-pass filtered (1/8–1/1.4 Hz) vertical-component waveforms and envelopes for 8 selected events. P- and S-wave arrivals are relatively easily picked on the vertical and horizontal components (see Supplementary Material (SM) Figs. S1 and S2), but alternative methods for detecting/identifying additional seismic phase arrivals are required. Moreover, Martian seismic data typically contain glitches, which represent transient one-sided pulses often accompanied by spikes that cover a wide frequency range (Scholz et al., 2020) (represented by dotted lines in Fig. 3) that require careful analysis to avoid pitfalls and false interpretations (Kim et al., 2021a).

A particular approach that has proven fruitful for the identification of seismic phases is the use of time-domain envelopes (Khan et al., 2021). We filter the data in narrow frequency bands and compute the envelopes of the time series. This allows us to better visualize energy partitioning across the different frequency bands and enables us to 1) determine the frequency bands where the energy related to seismic

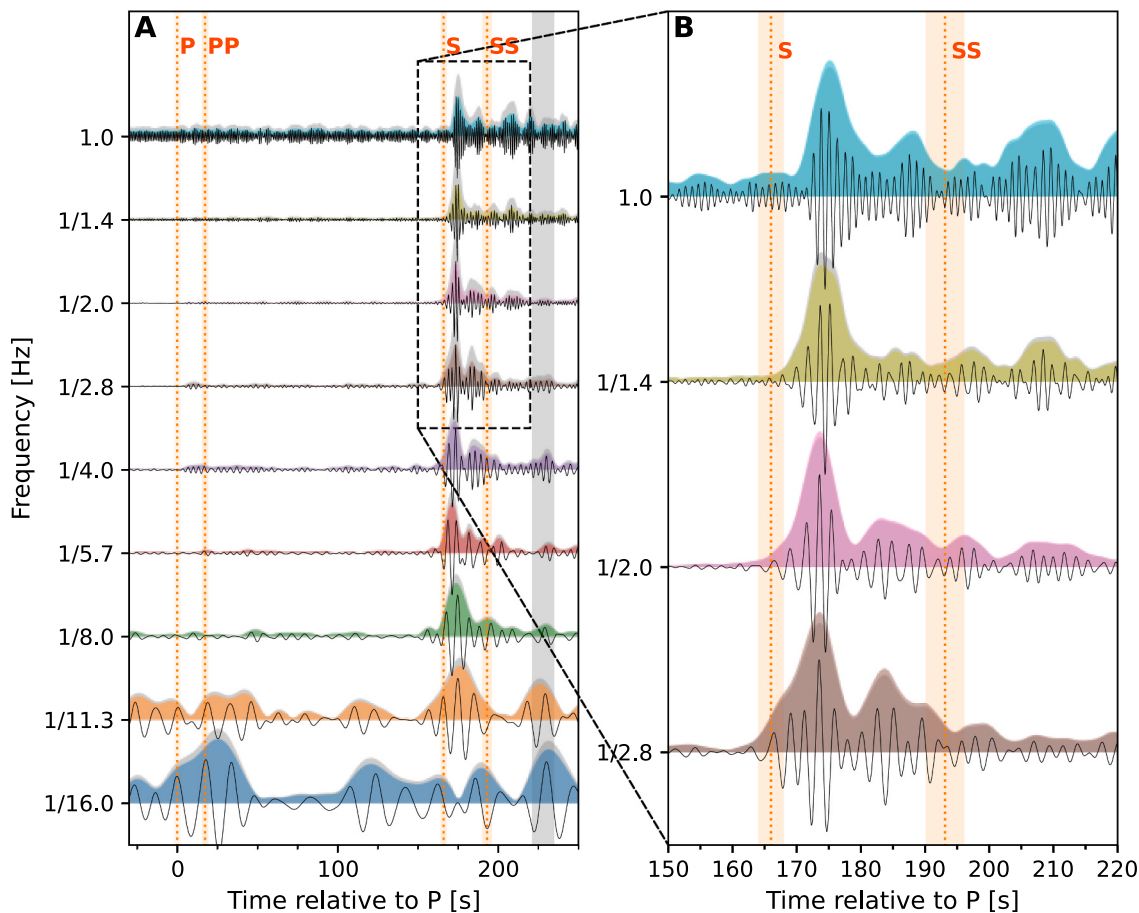


**Fig. 6.** Transverse-component time-domain envelopes and polarised traces for event S0235b across different frequency bands (filter banks). Time-domain envelopes are shown in grey. Polarised traces and their envelopes are shown in black (lines) and colour, respectively. Initial seismic phase picks for S0235b are shown as vertical dotted lines. Orange bars indicate uncertainties on the arrival time picks. Vertical grey bar represents a glitch. Panel (B) shows a zoomed-in version of the S-wave phases in (A). Amplitudes of traces and envelopes are normalized by their maxima and scaled for better visualisation.

phases is present, and 2) differentiate seismic from wind- or glitch-related signals.

For each event, velocity traces are rotated to the vertical-North-East (ZNE) system and band-pass filtered with a zero-phase-shift filter using a bandwidth half an octave wide around each central frequency, ranging from 1/16 Hz to 1 Hz. The selected filter banks cover the frequency bands where the events are most visible and are generally devoid of glitch- or wind-related artefacts (Scholz et al., 2020). For the events for which we can rely on back-azimuth estimations, velocity traces are further rotated to the vertical-radial-transverse (ZRT) system. This is exemplified for event S0235b as shown in Fig. 4, where we depict traces filtered in a broad frequency range (1/16–1 Hz) in black (bottom) and for the different filter banks in blue for the Z, R and T components. For this particular event, a glitch around 220 s after the P-wave arrival is present, affecting the waveforms on the horizontal components. From the narrow filter bands, we see that the glitch has no influence on the waveforms at frequencies above 1/5.7 Hz.

To compute envelopes, which better depict arrivals of energy packages, we add the squared amplitudes of the trace and its Hilbert-transform by considering 5-s long time windows, and then take the square-root. The envelopes are shown in Fig. 4 (in grey) with the correspondingly-filtered traces. Well-defined packages of energy are observed in the envelopes after the P- and S-wave arrivals, and they are particularly consistent for frequencies ranging from 1/5.7 to 1/1.4 Hz. Some of these packages, which could be related to the arrival of reflected body wave energy, are more pronounced in specific frequency bands. For instance, potential reflected P-wave arrivals are observed in the P-

wave coda in the Z component at frequencies of 1/1.4 and 1/2 Hz (indicated by arrows in Fig. 4A). The selection of reflected body wave arrivals based on time-domain envelopes is done jointly with polarised traces and their envelopes as described next.

#### 4.1.2. Polarised traces and their time-domain envelopes

Since particle motion coincides with the azimuth of propagation of energy for P-waves and is perpendicular to the azimuth of propagation for S-waves, compressional and shear waves exhibit a high degree of linear polarisation. On Earth, the microseismic background noise has been demonstrated to be elliptically polarised with little preferred directionality, as observed, for e.g., surface waves (Haubrich et al., 1963; Tanimoto et al., 2006). By using these characteristics of polarised particle trajectories, filters that preserve a certain particle motion can be applied.

To exploit the directionality and rectilinearity of body waves, we apply a time-domain polarisation filter that increases the SNR of the linearly polarised part of the signal that involves body-wave phases (Montalbetti and Kanasewich, 1970). With this method, information about the particle motion is obtained from the co-variance matrix of three-component seismograms over 5-s time intervals. Different window lengths were tested but were found to result in little change. By diagonalizing the matrix, the rectilinearity of the particle motion trajectory can be estimated from the ratio of the principal axes, while the direction of polarisation is found from the eigenvector of the largest principal axis. Traces are therefore filtered using the rectilinearity and directionality of compressional and shear waves to suppress energy associated with

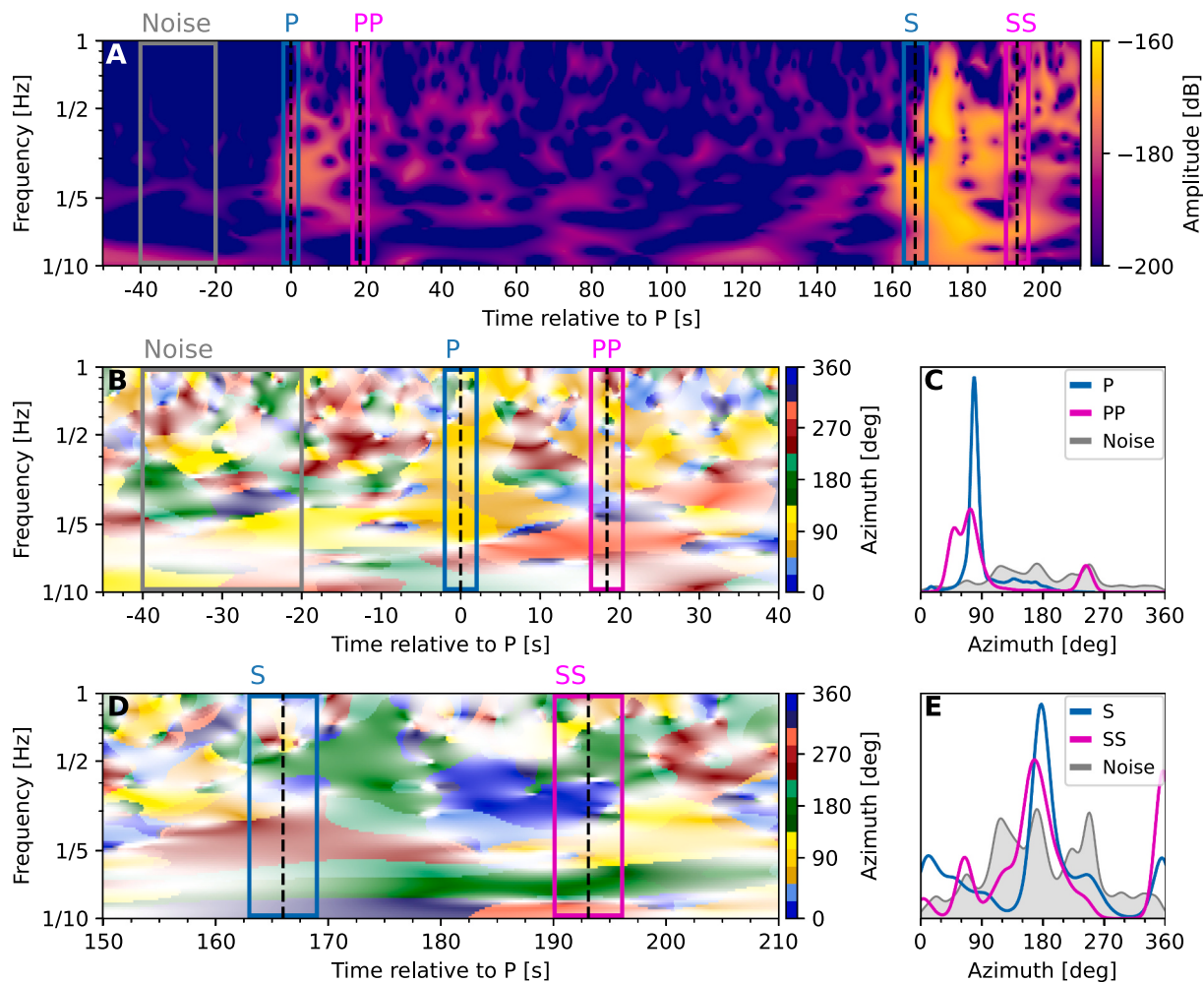


**Fig. 7.** Polarisation analysis for event S0235b. Panel (A) shows a time-frequency plot of the amplitude of the event, with framed windows indicating noise, P-, PP-, S-, and SS-wave arrivals. Azimuthal directions for a time window including pre-event noise and P-wave phases are shown in panel (B), while panel (D) exhibits azimuthal directions of S-wave phases. Panels (C) and (E) show density estimates of the selected P- (B) and S-wave phases (D) in the 0.3–1 Hz frequency band, including the pre-event noise for comparison.

background noise, with the objective of enhancing body-wave phases while smoothing-out elliptically-polarised signals.

We apply the time-domain polarisation filter to the band-pass filtered waveforms of each filter bank (section 4.1.1). Filtered polarised Z- and T-component traces for event S0235b are shown as black lines in Fig. 5 and Fig. 6, respectively. These polarised traces, in contrast to the raw traces shown in Fig. 3, clearly exhibit arrival of additional body waves (see Fig. 5B and Fig. 6B). To easily detect energy arrivals, envelopes are computed and depicted in Figs. 5 and 6 for the Z and T components, respectively (see SM Fig. S3 for R-component analysis). The polarised waveforms and their envelopes are overlapped with the time-domain envelopes (grey) described in section 4.1.1.

Whenever possible, discrete energy onsets are identified as seismic phases in the data, based on the time-domain envelopes and the polarised traces/envelopes. To qualify as seismic phases, arrivals must be present 1) across different frequency bands and 2) in both time-domain envelopes and polarised traces. This is illustrated in Fig. 5A, where the selected P-wave arrival, indicated by a dotted orange line, is present across all analyzed frequency bands. The selected onset of energy corresponding to the P-wave arrival is easily observed in the grey and colored envelopes. When looking at the PP-phase, it appears clearer at frequencies ranging from 1/2 Hz to 1 Hz (see Fig. 5B). Analogous to the P-wave arrival, the selected S-wave arrival is present across all analyzed frequency bands (see Fig. 6A), while the reflected SS-phase is mostly

prominent at frequencies in the range from 1/2.8 Hz to 1 Hz (see Fig. 6B). Although additional consistent energy impulses are observed in the P- and S-wave coda, these signals are not considered to be reflected body wave phases, because they do not exhibit the expected differential travel-time difference between consecutive phases. This is exemplified with the phase labelled X in Fig. 5B, which could be interpreted as PPP. However, this results in a travel-time difference between PPP and PP that is larger than the difference between PP and P, which is, as noted, unexpected. An analogous procedure is applied to each of the 14 events, resulting in a set of initial picks that includes P-, PP-, S-, and SS-wave arrivals (see SM Figs. S4-S16). These initial picks are further analyzed using polarisation analysis as described in the following.

#### 4.1.3. Polarisation analysis

As a means of validating the selected seismic phases, we employ polarisation analysis based on the work of Schimmel and Gallart (2003) and Schimmel et al. (2011). The approach relies on the eigen-analysis of the spectral matrix built from the recorded three-component seismic data, that are transformed into the time-frequency domain using a continuous wavelet transformation (Kristeková et al., 2009).

The polarisation attributes can be inferred from the resulting best-fitting polarisation ellipse. The ellipticity is given by the ratio of the semi-minor to the semi-major axis of the polarisation ellipse with values between 0 and 1. Therefore, an ellipticity of 1 describes circular ground

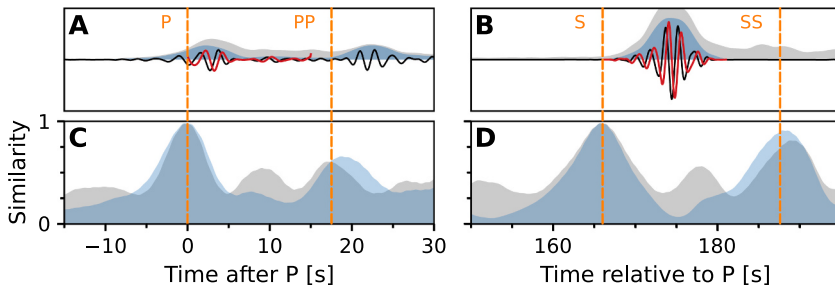


**Fig. 8.** Waveform matching analysis applied to event S0235b. Panels (A) and (B) show the time-domain envelopes (grey), polarised traces (black), and envelopes (blue) for the Vertical and Transverse components that are filtered in a narrow band centered at 1/2 Hz and at 1/1.4 Hz, respectively. Red traces in (A) and (B) indicate the 15-s long Hilbert transformed P- and S-waveforms employed to compute the similarity coefficients shown in (C) and (D). Panels (C) and (D) show the envelopes of the similarity coefficient for the polarised (blue) and non-polarised (grey) traces. Selected direct (P and S) and reflected (PP and SS) body-wave arrival picks are shown as vertical dashed lines. (For interpretation of the references to colour in this figure legend, the reader is referred to the web version of this article.)

motion, whereas low ellipticity values describe rectilinear motion. The orientation of the semi-major axis provides information on inclination as well as back-azimuth. The former is given by the deviation from the horizontal plane, while the latter is obtained from the projection of the axis onto the horizontal plane. Both inclination and back-azimuth are better constrained for rectilinear signals, as the semi-major axis is more stable.

We use a degree-of-polarisation filter following Samson (1983), which masks signals that are not strongly polarised, in addition to a filter based on ellipticity. For instance, we expect an incoming P-wave to be rectilinear and have a particle motion along the direction of the back-azimuth, while an S-wave is expected to arrive with a 90° (for SH) or 180° (for SV) shift in azimuth with respect to the P-wave.

Once initial seismic phases have been identified (see sections 4.1.1 and 4.1.2), we apply the polarisation analysis to the three-component seismic data for each event, focusing on windows around the selected arrivals and with a width given by the pick uncertainty. Polarisation analysis applied to the selected P-, PP-, S-, and SS-wave arrivals for event S0235b is illustrated in Fig. 7. A time-frequency plot of the signal amplitude is shown in Fig. 7A, with a 20 s pre-event noise window (grey-bounded box) for comparison with the P-, PP-, S-, and SS-phase arrival windows (blue- and pink-bounded boxes). The selected window for the P-wave arrival exhibits amplitudes that are significantly above background noise, with peak values for the P-wave arrival around -170 dB, while for the S-wave arrival, amplitudes reach -160 dB. Fig. 7B shows the azimuth of the semi-major axis of the polarisation ellipse using different colors for the signal in a time window that includes pre-event noise and P-wave coda. For the selected P- and PP-arrival time windows, the signal is consistent and dominated by azimuths close to 90° (yellow scale), especially in the frequency range in which the phase arrivals were picked (1/5.7 Hz–1 Hz). For comparison, no dominant azimuth is observed in the noise window. To further quantify this, we computed the azimuthal probability density for each of the three selected time windows in the 0.3–1 Hz frequency band (Fig. 7C) by marginalising over the frequency and time axes in Fig. 7B. The resultant azimuthal probability density curves for the P- and PP-wave arrival time windows are both maximum just below 90° (blue and pink bold lines in Fig. 7C), while, as expected, there is no preferred azimuthal direction for the pre-event noise window (grey bold line in Fig. 7C). Analogous to the P-wave arrivals, Fig. 7D and E show the azimuthal direction of the S- and SS-wave arrivals. In Fig. 7D, both S- and SS-wave arrivals show a consistent azimuth around 180° (green scale) for frequencies ranging from 1/2.8 Hz to 1 Hz. This is further corroborated through the azimuthal probability density curves in the 0.3–1 Hz frequency band that indicate a preferred azimuthal direction close to 180° for both S-wave arrivals.

When consistency in the polarisation of the chosen windows is observed (i.e., same direction of particle motion for all P-wave phases and for S-wave phases but with a 90-degree shift with respect to the compressional arrivals), the corresponding phases are selected. Body-wave arrivals that do not exhibit agreement with the main phase, for instance a PP-phase that is associated with a different azimuth than the one observed for the P-wave arrival, are removed.

#### 4.1.4. Waveform matching

When a seismic pulse propagates through the subsurface, it may be distorted by a variety of mechanisms. For example, after a surface-reflection, body-wave arrivals will undergo pulse distortion due to a shift in phase of each frequency component (Choy and Richards, 1975). The pulse deformation incurred at every surface-reflection was shown to be a constant  $\pi/2$  phase shift (Jeffreys and Lapwood, 1957). Thus, the outgoing reflected waveform is equivalent to a Hilbert transform of the incident P- or S-wave. For instance, an SS-wave resembles the Hilbert transform of the S-wave, while a second Hilbert transform would be representative of an SSS-wave (similarly for PP and PPP). In this study, we use the fact that direct and surface-reflected waves are related by a constant phase shift as an independent means to verify our phase arrivals.

For each event, we consider the frequency bands in which surface-reflected body-wave arrivals were selected (e.g., for event S0235b and the PP-wave arrival, they include frequencies ranging from 1/2 Hz to 1 Hz as shown in Fig. 5) and compute the Hilbert transform of a 15-s long window that includes the direct P- or S-wave arrival (hereinafter referred to as template trace). Following this, we cross-correlate the event trace with the template trace, considering lags every 0.05 s. The cross-correlation function  $\chi$  at every lag is given by

$$\chi(k) = \sum_{i=0}^{N_x-1} x_i y_{i+k}^* \quad (1)$$

where  $x$  and  $y$  are event and template traces, respectively,  $N_x$  and  $N_y$  the lengths of  $x$  and  $y$ , respectively,  $N = \max(N_x, N_y)$ , and  $k$  runs from 0 to  $N_x + N_y - 2$ . Subsequently, at every lag, we compute a similarity coefficient defined by the mean of the cross-correlation function. This coefficient represents the similitude between the event trace and the Hilbert transform of the direct P- or S-wave, and is equal to 1 in the case of perfect matching, and -1 when encountering the same waveform with opposite polarity. Since a change of polarity occurs when waveforms are reflected at the surface, we compute the absolute value of the similarity, with 1 representing perfect correlation (including opposite polarity) and 0 indicating completely uncorrelated traces. We apply this analysis to and seek high-similarity values for both, polarised and non-polarised, waveforms.

Application of the method to event S0235b is illustrated in Fig. 8. Fig. 8A and B show the Z- and T-component traces, respectively. For the Z component, we consider a frequency band centered at 1/2 Hz, while for the T component we consider a frequency band centered at 1/1.4 Hz. Grey-shaded curves represent the time-domain envelopes, while black waveforms and blue-shaded curves represent the polarised traces and their envelopes. Superimposed are the template traces (in red): the Hilbert transform of the polarised direct P- and S-waves. Grey- and blue-shaded curves in Fig. 8C and D represent the envelopes of the similarity curve obtained using non-polarised and polarised traces, respectively. For comparison, body-wave arrivals selected with the methods described in the previous sections are indicated by the vertical dashed orange lines. Fig. 8C and D exhibit a clear increase of similarity around

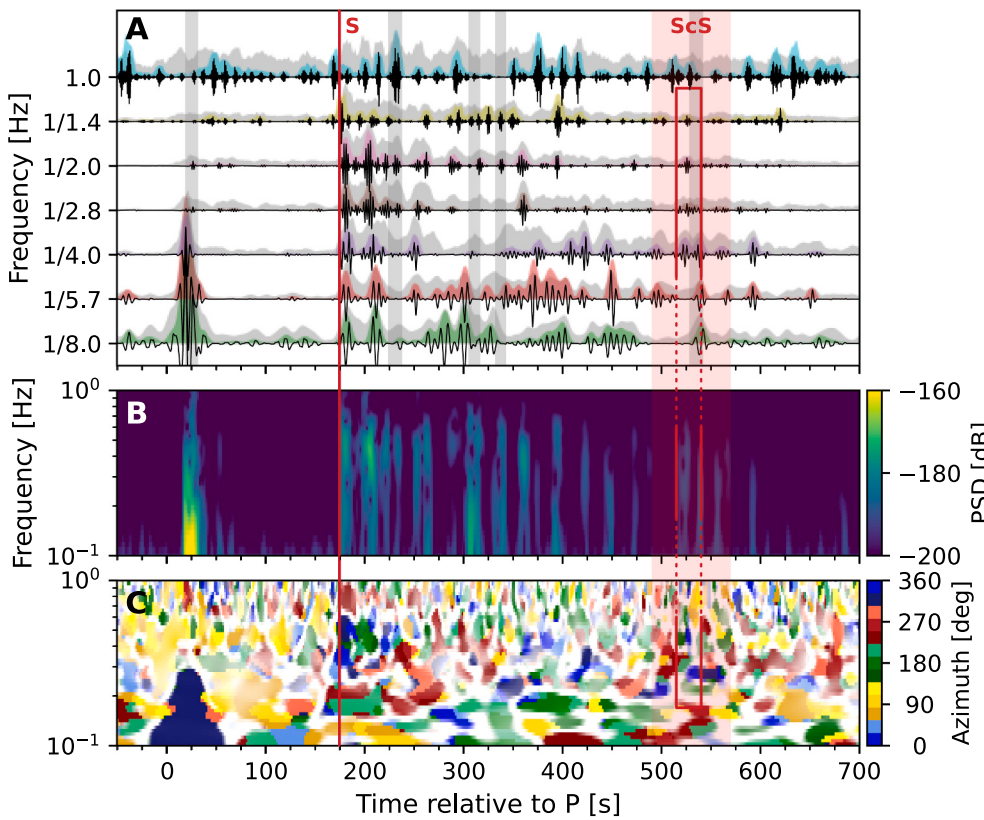


**Fig. 9.** Transverse-component time-domain envelopes and polarised traces across different frequency bands (filter banks) (A), spectrogram (B), and polarisation analysis (C) for event S0173a. (A) Time-domain envelopes are shown in grey, while polarised traces and their envelopes are shown in black (lines) and colour, respectively. Vertical grey bars indicate glitches. Amplitudes of traces and envelopes are normalized by their maxima and scaled for better visualisation. The red vertical bar indicates predicted arrival time range for ScS based on pre-mission models and the red box shows the window in which the ScS arrival is picked. The red vertical line shows the selected S-wave arrival. (For interpretation of the references to colour in this figure legend, the reader is referred to the web version of this article.)

the selected PP- and SS-wave arrivals for both, polarised and non-polarised, traces, respectively, indicating a close resemblance between the template trace and the event trace.

The waveform matching method provides an independent means of verifying body-wave arrivals by seeking similarity between the surface-reflected body-waves and the Hilbert transform of the direct body-waves (Khan et al., 2021). This method allows us to clearly identify the phase shift and corroborate the selected body-wave arrivals for the highest SNR events: S0167b, S0173a, S0325a, S0484b, and S0809a (see SM Figs. S17–S21).

#### 4.2. Seismic phase identification: core-reflected body waves

The direct and reflected seismic body waves identified hitherto mostly sample the crust and upper mantle of Mars (Khan et al., 2021). To include data that bear directly on the deep interior structure, we consider observations of core-reflected phases.

Pre-InSight constraints on the core of Mars relied on global geophysical measurements (tidal response and mean mass and moment of inertia) and geochemical analyses of Martian rocks that suggested a liquid core with a radius in the range 1700–1900 km (Khan et al., 2018; Smrekar et al., 2019; Konopliv et al., 2020; Bagheri et al., 2019; Rivoldini et al., 2011). These estimations constrain the expected travel times for core-reflected body waves. Here, we implement the techniques described in sections 4.1.1–4.1.3 to detect potential core-reflected P- and S-waves relying on the aforementioned Martian core radius range.

We compute time-domain envelopes and polarised traces for different filter banks for the 14 selected events and overlay them with the predicted travel times of core-reflected P- and S-waves. To compute the predicted travel times, we consider Martian candidate models (Clinton et al., 2017; Khan et al., 2021) with core radii in the pre-InSight range 1700–1900 km and predict travel times for core-reflected phases using the TauP toolkit (Crotwell et al., 1999). The resultant travel-time distributions allow us to confine the range within which core-reflected

arrivals are expected.

S-waves reflected at the core-mantle-boundary (ScS and PcS phases) are expected to be predominantly horizontally polarised at the receiver. We therefore look for seismic phases that are strongly linearly polarised in the horizontal direction. For core-reflected P-waves (PcP and ScP), we follow an analogous approach and seek vertically polarised arrivals. Because of attenuation, strong scattering, and interfering phases (Giardini et al., 2020; Lognonné et al., 2020), the SNR for core-reflected phases is generally low, rendering the identification of core-reflected body-wave arrivals difficult.

Of the 14 LF events considered in this study, only S0173a provides a confident enough identification of a core-reflected arrival. The T-component time-domain envelopes and polarised traces of this event are shown in Fig. 9A. The red-shaded area marked as ScS represents the arrival time range based on the predictions for a core radius ranging from 1700 to 1900 km. We observe a strong arrival compatible with ScS in the frequency range from 1/4–1/1.4 Hz (red box), occurring on the same component as the S-wave arrival. A spectrogram of the polarised trace is computed and shown in Fig. 9B, displaying a robust and clear increase of energy around the selected ScS arrival.

To strengthen the interpretation of the selected ScS arrival, the polarisation analysis method is applied to the traces and the results are shown in Fig. 9C. Since core-reflected arrivals are expected to arrive with a high incidence angle, we filtered data by inclination as a means of further improving their detection. This technique confirms the presence of a strongly polarised signal at the location of the selected ScS arrival, with an azimuth consistent with that observed for the S-wave arrival. Azimuthal probability density curves for both S- and ScS-wave arrivals are shown in SM Fig. S22. Finally, Z-component time-domain envelopes and polarised traces for S0173a were analyzed for core-reflected P-waves analogously to ScS, but the low SNR observed in the Z-component prevents us from identifying an arrival (see SM Fig. S23).

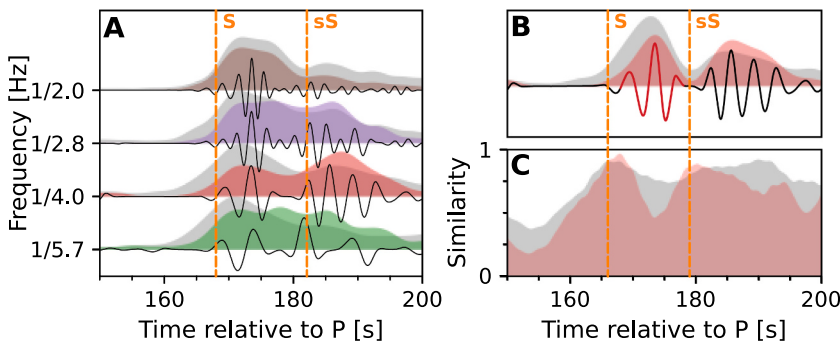


**Fig. 10.** Transverse-component time-domain envelopes and polarised traces across different frequency bands (filter banks) (A) for event S0235b. Time-domain envelopes are shown in grey, while polarised traces and their envelopes are shown in black (lines) and colour, respectively. Panels (B) and (C) illustrate the waveform matching analysis applied to the S-wave on the Transverse component in a frequency band centered at 1/4 Hz. Template and event trace are shown in red and black in panel (B), respectively. Vertical dashed lines indicate the selected S- and sS-wave arrivals. (For interpretation of the references to colour in this figure legend, the reader is referred to the web version of this article.)

**Table 1**

Observed body-wave differential travel times for the seismic phases identified in stage 1. Seismic arrival picks are made based on visual inspection of time-domain envelopes, polarised traces, and polarisation analysis. Tabulated times are expressed in seconds after the main P-wave arrival. Absolute P-wave arrival times (UTC) are listed in Table S2. In the case of the low-frequency event family, and for a handful of high-amplitude events, onsets may be identified in the time domain, but generally uncertainties on individual arrivals are assigned using the time-domain filter banks and the polarised traces and typically range between 1 and 5 s for the initial set of picks.

Event	$T_{pp}$	$T_{pp}$	$T_s$	$T_{ss}$	$T_{ss}$	$T_{sS}$
S0167b	–	$37.0 \pm$ 3	$414.5 \pm$ 2	–	$468.0 \pm$ 3	–
S0173a	$11.1 \pm$ 3	–	$174.8 \pm$ 2	$184.8 \pm$ 3	$197.9 \pm$ 2	$515.0 \pm$ 5
S0183a	–	$24.5 \pm$ 4	–	–	–	–
S0185a	–	–	$360.2 \pm$ 2	$379.5 \pm$ 4	$402.4 \pm$ 3	–
S0235b	–	$17.4 \pm$ 2	$166.0 \pm$ 3	$178.7 \pm$ 3	$193.1 \pm$ 3	–
S0325a	$11.3 \pm$ 3	$23.0 \pm$ 5	$230.7 \pm$ 3	–	$260.7 \pm$ 4	–
S0407a	–	–	$172.2 \pm$ 2	$183.4 \pm$ 3	–	–
S0409d	–	–	$162.5 \pm$ 3	–	–	–
S0484b	–	$18.1 \pm$ 5	$170.2 \pm$ 1	$184.0 \pm$ 3	$196.8 \pm$ 3	–
S0784a	–	$15.2 \pm$ 4	$173.0 \pm$ 4	$182.2 \pm$ 4	$196.9 \pm$ 5	–
S0802a	–	–	$176.5 \pm$ 5	–	–	–
S0809a	–	$15.5 \pm$ 5	$175.0 \pm$ 1	–	$197.6 \pm$ 3	–
S0820a	–	–	$176.0 \pm$ 2	$186.2 \pm$ 3	–	–
S0864a	–	$18.0 \pm$ 5	$169.0 \pm$ 3	$181.2 \pm$ 4	$194.0 \pm$ 3	–

#### 4.3. Seismic phase identification: depth phases

In addition to the body-wave phase arrivals analyzed in the preceding sections, near-source reflections of P- and S-wave arrivals, such as pP and sS (referred to as depth phases), can also be observed in the martian seismograms. Since these phases follow approximately the same path as the main P- and S-waves, the relative time delay between a depth phase and its associated principal phase (i.e.,  $T_{pp}-T_p$  and  $T_{ss}-T_s$ ) provides a constraint on the travel time between the source and the surface. Therefore, for a known velocity structure and epicentral distance, depth phases allow us to determine event depth.

To illustrate the selection of depth phases, we consider the sS-wave arrival for event S0235b. Since the S-wave arrival was picked on the T component (Fig. 6), we also look for the depth phase there. Fig. 10A shows the T-component time-domain envelopes and polarised traces for

event S0235b across different filter banks in the vicinity of the S-wave arrival. A second strong arrival immediately after the S-wave is clearly discernable in the frequency range 1/5.7–1/2.0 Hz with a frequency content similar to that of the S-wave, which we pick as the sS phase.

As a means of validating our selection, we apply the waveform matching method. The grey-shaded area in Fig. 10B represents the time-domain envelope, while the black waveform and red-shaded area represent the polarised trace and its envelope (filtered in a frequency band centered at 1/4 Hz, where the depth phase is most conspicuous). To compute the similarity curve, we consider the first 10 s of the S-wave arrival (red curve, Fig. 10B) as template to avoid including surface reflections. The envelopes of the similarity curve obtained by employing both non-polarised and polarised traces are represented by grey- and red-shaded areas in Fig. 10C, respectively. A clear increase in similarity around the selected sS-wave arrival, particularly for the polarised trace, is evident in Fig. 10C, which indicates that the S-wave (template trace) and the sS-wave, are highly similar.

Proceeding in this manner, we identify depth phases for 9 of the 14 analyzed events. For the events for which no depth phases could be identified, we fix depth to the mean of all observed depth phases (31.2 km).

#### 4.4. Summary of initial body-wave picks

The set of initial differential travel times (all times are relative to the main P-wave arrival) selected after the application of the different techniques just described are tabulated in Table 1 and illustrated in Fig. 11. In Fig. 11, picks of events are aligned by the observed S-P travel time difference ( $T_s-T_p$ ), with the exception of event S0183a for which no S-wave is observed and the distance is obtained based on the differential travel time between compressional waves. The differential travel times shown in Fig. 11 represent our preliminary data set that we invert for epicentral distance and interior structure, while predicting travel times of additional phases. Uncertainties on individual arrivals are assigned using the time-domain filter banks and the polarised traces and typically range between 1 and 5 s for the initial set of picks.

#### 4.5. Seismic phase identification: converted body waves

The fundamental idea of the receiver function (RF) method is to separate signals generated by the direct and converted phases on three-component ground-motion recordings based on their distinct particle motion (e.g., Rondenay (2009)). In the case of the Ps RF, they record compressional waves that convert into shear waves when encountering a discontinuity in material properties, while the order is reversed for the Sp RF. As a consequence, deconvolving the direct phase (direct wavefield) from the converted phase results in a time series representing the local structural response (Vinnik, 1977; Langston, 1979). Source and path effects between event and conversion point are ideally removed through deconvolution since they are contained in both, source and response, traces (Kind et al., 2012).

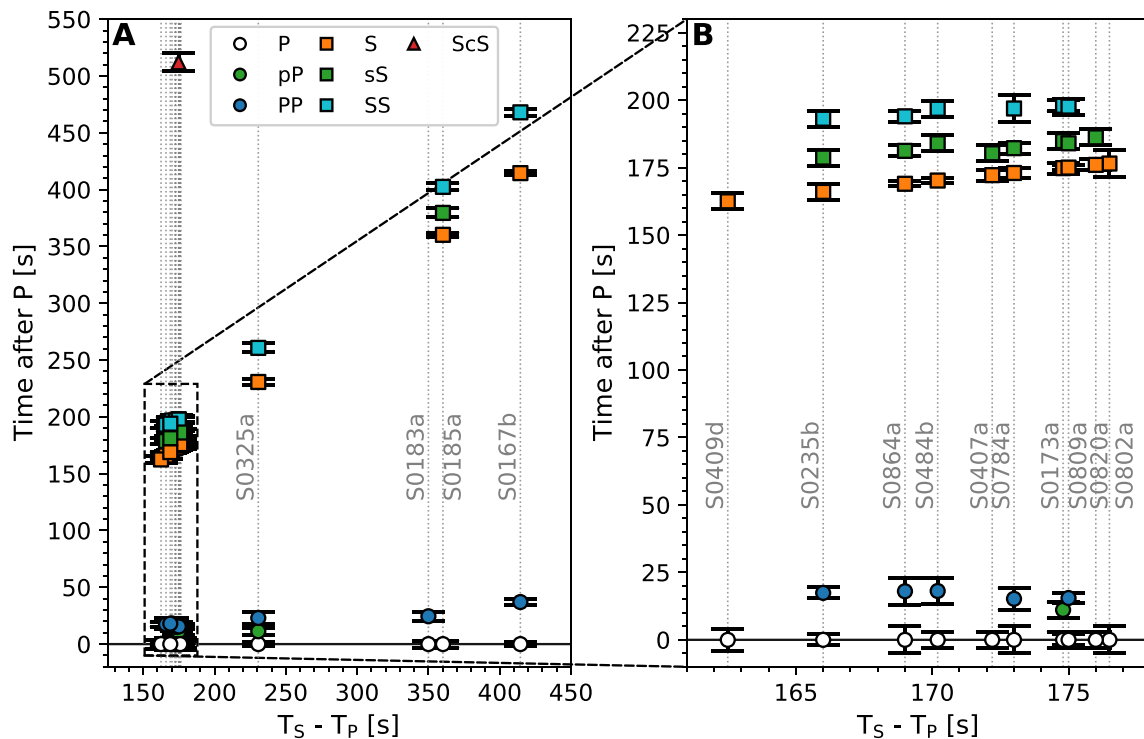


**Fig. 11.** Differential travel time plot based on the first set of body wave picks (see Table 1). Error bars indicate the uncertainties on the different seismic phases. Panel (A) shows all the seismic phases picked, while panel (B) shows a zoomed-in version for the events clustered around an S-P travel time difference of 170 s.

For near-vertical incidence, the P-wave motion is primarily recorded on the Z component and the converted wave on the radial component. However, rotation of the traces into the ZRT system requires knowledge about the back-azimuth of the marsquake, which limits the amount of events usable for computing RFs. Here we focus on the events for which either estimations of back-azimuth are available (Clinton et al., 2021) or clear body wave polarisation is observed (based on the azimuthal direction of signals described in section 4.1.3): S0173a, S0183a, S0235b, S0784a, S0802a, S0820a, and S0864a.

#### 4.5.1. Receiver function processing

In order to compute RFs, we follow a processing scheme similar to Method C of Knapmeyer-Endrun et al. (2021). For each event, waveforms are tapered and band-pass filtered between 2 s and 5 s, and then rotated to the ZRT-system on the basis of the estimated back-azimuths. Traces

are subsequently rotated to the LQT-system, where the L component is aligned in the direction of P-wave propagation and Q in the direction of SV-wave displacement. Rotation to this system allows to further separate P- and S-wave energy, increasing the detectability of the converted waves (Rondenay, 2009; Kind et al., 2012). Rotation is achieved via principal component analysis, minimizing the energy on the R/Z-component in a 30-s time window around the P- and S-wave arrivals in the case of Ps RFs and Sp RFs, respectively. P- and S-wave arrival time estimations follows the procedure laid out in section 4.1.

To compute the RFs, we apply iterative time-domain deconvolution (Ligorría and Ammon, 1999), deconvolving source from response waveform. The source wavelet is extracted by trimming the corresponding trace around the picked arrival of the direct phase within  $-10$  s to  $+50$  s and from  $-100$  s to  $+20$  s for Ps and Sp RFs, respectively; while the response trace is obtained by trimming the waveforms within a

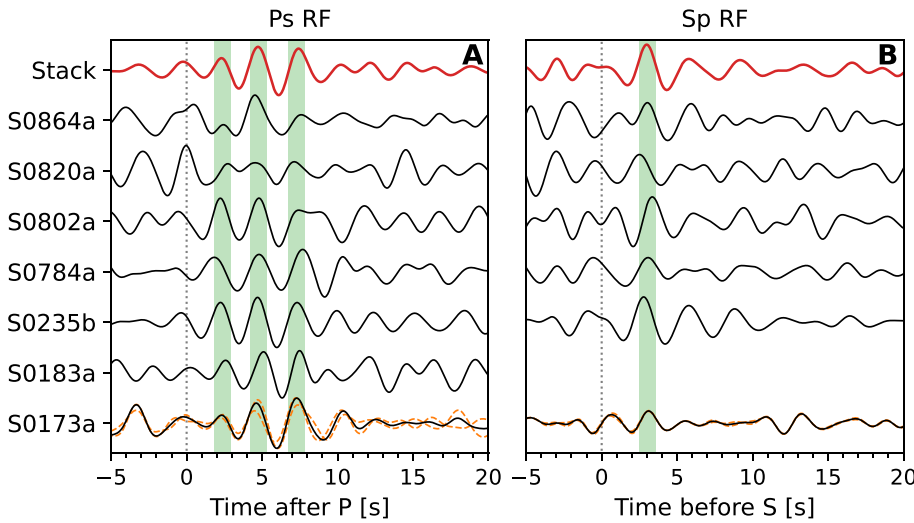


**Fig. 12.** Observed Ps (A) and Sp (B) receiver functions (RF) for the events indicated to the left of panel (A). The RFs are filtered between 2 s and 5 s and stacked to produce the final RF (top most trace). Green vertical bars indicate phases that are consistent across events. The RF for event S0173a is constructed as the stack of the RF of the different deglitched traces (orange dashed lines at the bottom). (For interpretation of the references to colour in this figure legend, the reader is referred to the web version of this article.)

window from  $-10$  s to  $+50$  s and  $-150$  s to  $+20$  s for Ps and Sp, respectively. Different source and response windows were tested, but their influence on the final RF were found to be negligible. Our processing method mainly differs from the one of Knapmeyer-Endrun et al. (2021) in the employed frequency ranges and the window lengths considered when deconvolving. The RFs for each event, with the exception of Sp for event S0183a, for which no clear S-wave arrival is observed, are illustrated in Fig. 12. For comparison with the Ps RFs, the time axis of the Sp RFs is flipped. For event S0173a, glitches are present, and we employ the deglitched data set of Scholz et al. (2020), which requires computing the RF for each deglitched data set and thereafter stack the different deglitched RFs into a unique RF representative of the event.

In order to ensure that information from many events are combined coherently, RFs are stacked into a single trace representative of the structure below the station. The results are shown in Fig. 12, where the stacked RFs for Ps and Sp are represented in red. The Ps RFs show three consistent positive arrivals within the first 8 s (green bands in Fig. 12), which are also visible in the individual RFs. No clear and consistent later phase is observed. Due to the timing of the observed arrivals, they are mainly sensitive to crustal structure. Since most events are located at epicentral distances between  $27^\circ$  and  $32^\circ$ , no move-out of either the direct arrivals or the multiple reflections is expected, and no move-out correction is applied.

The stacked Sp RF, in contrast to the Ps RF, contains a single dominant arrival around 3 s, in agreement with earlier results of Knapmeyer-Endrun et al. (2021); Kim et al. (2021b). However, the phase is not clearly identifiable in most individual event traces, since additional arrivals are comparable in amplitude. The use of the Sp RF for making structural inferences is limited in relation to Ps RFs, as pointed out by Bissig et al. (2021), because it includes a range of interfering phases, which complicates observations of Sp conversions. As a consequence, we do not employ the Sp RF when inverting for crustal structure, but use it in a predictive sense.

In summary, the final set of data employed to constrain the crustal structure in stage 1 consists of the stacked Ps RF, within a window ranging from 0 to 8.6 s (including the aforementioned three consistent arrivals) and the differential travel times (Table 1) obtained following the procedure outlined in section 4.1.

## 5. Model parameterisation and forward modelling

### 5.1. Geophysical model parameterization

We follow the geophysical parameterization of Khan et al. (2021) and consider a spherically symmetric model of Mars, divided into crust, mantle, and core. Crustal structure is parameterized in terms of three layers with variable S-wave velocity  $V_S^i$  and thickness  $d_i$ . Crustal S-wave velocities are assumed to increase as a function of depth ( $V_S^i < V_S^{i+1}$ ), while density and P-wave velocity are scaled to S-wave velocity using variable but depth-independent scaling factors. For the sub-lithospheric mantle, we compute radial profiles of seismic P- and S-wave velocity and density using phase equilibria computations in the CaO-FeO-MgO-Al<sub>2</sub>O<sub>3</sub>-SiO<sub>2</sub>-NaO<sub>2</sub> (CFMASNa) model chemical system. The stable mantle mineralogy and physical properties are computed employing Gibbs free-energy minimization and equation-of-state modelling (Connolly, 2009) as a function of temperature, pressure, and composition, using the thermodynamic formulation and parameters described in Stixrude and Lithgow-Bertelloni (2005, 2011). The lithospheric thermal structure is described by a conductive geothermal gradient between the crust-mantle interface (variable) and the bottom of the lithosphere (variable), while the sublithospheric mantle is assumed adiabatic. We computed mantle adiabats (isentropes) self-consistently from the entropy of the lithology at the pressure and temperature of the bottom of the thermal lithosphere. The mantle pressure profile is obtained by integrating the vertical load from the surface pressure boundary

**Table 2**

Major-element Martian mantle compositions from Khan et al. (2022). The compositions are expressed as ranges based on 10 randomly selected models that are representative of the model range derived by Khan et al. (2022). All numbers in wt%.

	CaO	FeO	MgO	Al <sub>2</sub> O <sub>3</sub>	SiO <sub>2</sub>	NaO <sub>2</sub>
AK21	2.2–3.2	12.7–14.9	31.2–36.0	3.2–3.8	43.4–47.5	0.3–1.3

**Table 3**

Overview of model parameters, prior model ranges, and prior probability distributions.

Description	Parameter	Quantity	Value/range	Distribution
Crustal properties	$V_S^i$	3	1.5–4.2 km/s	uniform
	$V_P^i$	–	$\alpha \cdot V_S^i$	$V_{S/P}^1 \leq V_{S/P}^2 \leq V_{S/P}^3$
	$\rho$	–	$\beta \cdot V_S^i$	$\rho^1 \leq \rho^2 \leq \rho^3$
$V_P/V_S$ scaling	$\alpha$	1	1.65–1.85	uniform
$\rho/V_S$ scaling	$\beta$	1	0.75–0.95	uniform
Crustal thickness	$\Delta Z_c$	1	20–60 km	uniform
Crustal layers thickness	$\Delta Z_i$	3	1–50 km	uniform
Lithospheric temperature	$T_{lit}$	1	1273–1873 K	uniform
Lithospheric depth (depth to intersection of conductive lithospheric geotherm and mantle diabat)	$Z_{lit}$	1	100–600 km	uniform
Mantle composition (in CFMASNa system)	$X_m$	–	see Table 2	fixed
Core radius	$R_{cmb}$	1	1500–2300 km	uniform
Core S content	$X_s$	1	0.05–0.5 wt %	uniform
Epicentral distance	$\Delta$	14	0°–180°	uniform
Source depth <sup>1</sup>	$h'$	10	10–100 km	uniform
Source depth <sup>2</sup>	$h$	4	–	fixed

<sup>1</sup> This includes the set of events for which depth phases could be identified: S0173a, S0185a, S0235b, S0325a, S0407a, S0484b, S0784a, S0820a, S0864a.

<sup>2</sup> This includes the set of events for which depth phases could not be identified: S0167b, S0183a, S0409d, S0802a, S0809a.

condition.

In what follows, we rely on the new model martian compositions of Khan et al. (2022) given in Table 2, that match the seismic, geophysical, and cosmo- and geochemical data. We further assume that the core is made of Fe-FeS, is entirely liquid, well-mixed, and convecting (Rivoldini et al., 2011; Khan et al., 2018; Bagheri et al., 2019). Thermoelastic properties for the core are computed using equation-of-state for liquid iron and liquid iron-sulfur alloys after Rivoldini et al. (2011). Core parameters include radius, sulfur content, and the input parameters required to compute physical properties (pressure and temperature at the core-mantle boundary). Pressure is determined by integrating the load from the surface to the core-mantle-boundary (CMB), while temperature is estimated from the entropy of the lithology at the bottom of the lithosphere. Prior model parameters and ranges are summarized in Table 3.

### 5.2. Seismic model parameterization

In order to provide an independent validation of our results, we follow Khan et al. (2021) and Stähler et al. (2021) and invert the differential travel time data employing a standard seismic parameterization. This parameterization considers a simplified layered model of Mars described by variable P- and S-wave velocity gradients. Layers in the

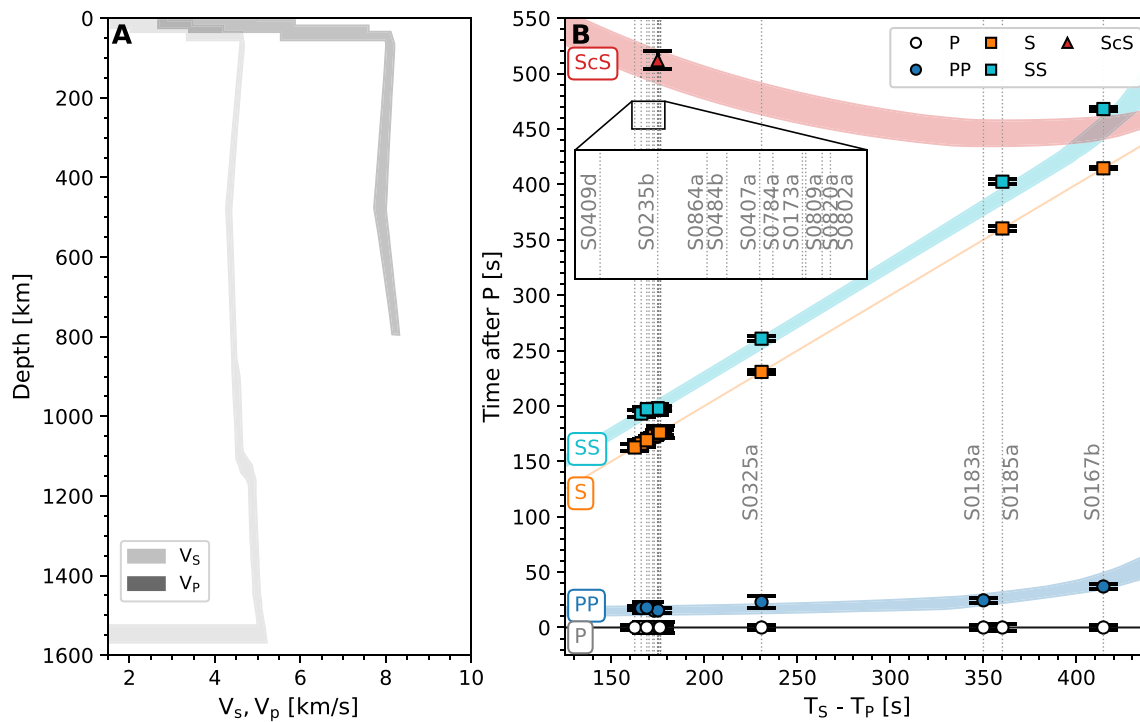


**Fig. 13.** Seismic wave velocity profiles (A) obtained from inversion of the initial set of differential travel time picks (Table 1) based on the geophysical parameterization (see section 5). Because there are no observations of P-waves that traverse the lower mantle, P-wave velocity below 800 km depth is not shown. (B) Differential body-wave travel time misfits for all models shown in (A).

crust are parameterized in terms of variable thickness and variable P-to-S velocity scaling, with velocities increasing as a function of depth. The mantle structure is described by variable depth nodes and independent P- and S-wave velocities that are free to sample an a priori velocity range (prior model parameter ranges are summarized in SM Table S1). The importance of this parameterisation is that it enables us to invert for model structure independently of mineral physics data, while also allowing for an increased flexibility in the determination of the velocity models. This parameterisation will be discussed further in the final inversion stage (section 7.3).

### 5.3. Estimating travel times

For each sampled velocity model, we employ the TauP toolkit Crotwell et al. (1999) to compute travel times. Since the event origin time is typically unknown, we use differential times relative to the P-wave arrival. In analogy to the approach of Khan et al. (2021), we simultaneously invert for epicentral distance of all events, which is mainly constrained by the differential travel time between P- and S-wave arrivals.

### 5.4. Synthetic receiver function modelling

In order to generate synthetic RFs for each event, we compute waveforms for the 7 LF events considered in section 4.5 using the reflectivity method (Fuchs and Müller, 1971; Müller, 1985). These synthetic waveforms are filtered, deconvolved, and stacked employing identical methods to those applied to the observed seismograms (section 4.5.1), ensuring consistency in processing between synthetic and observed RFs (Munch et al., 2018; Bissig et al., 2021). As the source influence is removed by deconvolution, the source characteristics do not have a significant effect on the synthetic RF waveforms. Hence, we model the source as an explosion, ensuring optimal radiation of P and SV waves, with a source-time function defined by a Heaviside function and depth given by the mean of the depth distribution of the observed

events. In contrast to the process applied to rotate the observed seismograms, which relies on a principal component analysis, we rotate the synthetic traces to the LQT-system using the theoretical incidence angle obtained from ray tracing.

## 6. Inverse problem

To solve the inverse problem, we employ the probabilistic approach of Mosegaard and Tarantola (1995). In this Bayesian formulation, the solution to the inverse problem  $\mathbf{d} = g(\mathbf{m})$ , where  $\mathbf{d}$  is a data vector containing observations and  $g$  is a typically non-linear operator that maps from the model to the data space, is given by the posterior probability distribution  $\sigma(\mathbf{m})$

$$\sigma(\mathbf{m}) = kf(\mathbf{m})\mathcal{L}(\mathbf{m}) \quad (2)$$

where  $k$  is a normalization constant,  $f(\mathbf{m})$  is the prior model parameter probability distribution and  $\mathcal{L}(\mathbf{m})$  is the likelihood function, which is a measure of the similarity between the observed data and the predictions from model  $\mathbf{m}$ . The particular form of  $\mathcal{L}(\mathbf{m})$  is determined by the observations, their uncertainties, and how these are employed to model data noise.

Assuming data noise is uncorrelated and described by a Laplacian distribution ( $L_1$ -norm), which is less prone to be affected by outliers than the  $L_2$ -norm (Khan and Mosegaard, 2002), the likelihood function takes the form

$$\mathcal{L}(\mathbf{m}) \propto \prod_{\nu} \exp(-\Phi^{\nu}), \quad (3)$$

where  $\Phi$  is the misfit function,  $\nu$  is either of the considered data set: stacked RF, differential travel times, mean density ( $\bar{\rho}$ ), and mean moment of inertia ( $I/MR^2$ ). The general expression for the misfit is

$$\Phi^{\nu} = \frac{1}{N} \sum_j^N \frac{|\mathbf{d}_{\text{obs}_j}^{\nu} - \mathbf{d}_{\text{cal}_j}^{\nu}|}{\sigma_j^{\nu}}. \quad (4)$$

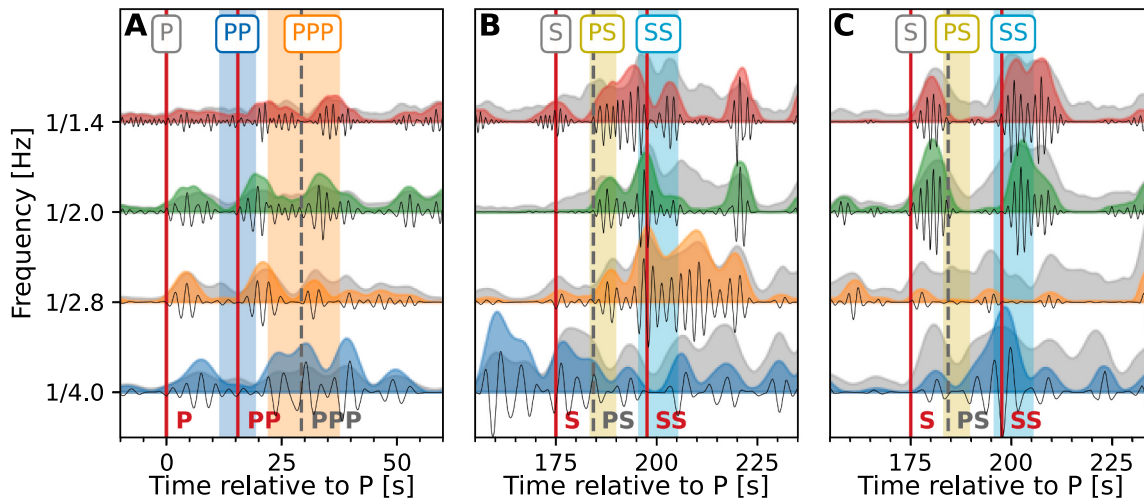


**Fig. 14.** Time-domain envelopes and polarised traces for event S0809a across different frequency bands (filter banks) for the vertical (A), north (B), and east (C) components. Time-domain envelopes are shown in grey and polarised traces and their envelopes are shown in black (lines) and colour, respectively. The vertical bands represent predictions of differential travel times from the inverted preliminary velocity models shown in Fig. 13 for a number of seismic phases that were not picked initially (vertical solid red lines) (Table 1), while grey dashed lines indicate new arrivals based on the predicted differential travel times. (For interpretation of the references to colour in this figure legend, the reader is referred to the web version of this article.)

- In the case of the stacked RF,  $\mathbf{d}_{\text{obs}}$  and  $\mathbf{d}_{\text{cal}}$  denote the vectors of observed and synthetic amplitudes of the stacked Ps RF, and  $\sigma$  the data uncertainty, with  $N$  expressing the total number of points within the misfit window. The uncertainty  $\sigma$  is set to 50% of the mean absolute Ps RF amplitude within the misfit window 0–8.7 s, covering the three main peaks of the RF signal (green vertical bands in Fig. 12A).
- For the differential travel times,  $\mathbf{d}_{\text{obs}}$  and  $\mathbf{d}_{\text{cal}}$  denote the vectors of observed and synthetic differential travel times, with  $N$  expressing the total number of differential travel times, which comprises all possible combinations of phases with respect to P and S:  $T_S - T_P$ ,  $T_{PP} - T_P$ ,  $T_{SS} - T_P$ , ...,  $T_{ScS} - T_S$ .
- In the case of  $I/MR^2$  and  $\bar{\rho}$ , we employ the latest observations of the mean moment of inertia  $I/MR^2 = 0.3638 \pm 0.0001$  and mean density  $\bar{\rho} = 3.935 \pm 0.0012 \text{ g/cm}^3$  (Rivoldini et al., 2011; Konopliv et al., 2020).

Finally, to sample the posterior distribution (Eq. 2), we employ the Metropolis algorithm (Mosegaard and Tarantola, 1995). This algorithm, which samples the model space in a random fashion, ensures that models that fit the data well and are simultaneously consistent with prior information are sampled more frequently. The sampling is performed using 15 independent chains, with each chain performing  $10^4$  iterations, resulting in a total of  $1.5 \times 10^5$  models. To ensure near-independent samples, every 50th model was retained.

## 7. Inversion results and consolidation of seismic phases

### 7.1. Stage 1: preliminary inversion

Following the initial identification of direct, surface- and core-reflected, and converted body-wave arrivals, we invert our initial differential travel time picks (Table 1) for a set of preliminary radial models of P- and S-wave speed, density, and source location (epicentral distance). The inverted seismic velocity models based on the geophysical parameterisation and their fit to the observed differential body-wave travel-time data are shown in Fig. 13. Because the predicted travel-time curves are plotted as a function of differential travel time (S-P), there is no model spread associated with the P- and S-wave travel-time curves as is the case for PP, SS, and ScS. The larger spread for ScS relative

to PP and SS simply reflects the fact that only a single observation is available. Our fit to the converted waves will be discussed below. Finally, preliminary epicentral distances obtained as part of the inversion are shown in Fig. S24.

### 7.2. Stage 2: iterative refinement - identifying additional arrivals

Based on the preliminary velocity models (Fig. 13A), we predict travel times for a series of body-wave phases (PP, PPP, PS, SS, SSS, P<sub>c</sub>S, and ScS) that could not be identified in stage 1. Note that we include PP, SS, and ScS in the list because for some events these phases were not picked initially. To hunt for these additional phases in the event seismograms, we employ the computed travel-time distributions and combine these with the time-domain envelopes and polarised traces discussed earlier (section 4.1).

#### 7.2.1. Surface-reflected phases

The procedure is illustrated in detail using event S0809a, for which P-, PP-, S- and SS-wave arrivals were determined in stage 1. Fig. 14 shows Z-, N-, and E-component time-domain envelopes and polarised traces for this event in the frequency range 1/4 Hz–1/1.4 Hz, which is the frequency range where the aforementioned phase arrivals were observed (see SM Fig. S14 for additional frequency ranges analyzed in stage 1 with time-domain envelopes and polarised traces). Vertical solid lines indicate the picks selected in stage 1 and vertical colored bands indicate the predicted travel times for the different body-wave phases.

Repeating the methodology applied in stage 1, we compute time-domain envelopes and polarised traces and envelopes, and combine these with the computed travel time distributions as shown in Fig. 14. Proceeding thus, we identify two additional phases, PPP and PS, that show strong energy arrivals in the frequency range from 1/2.8 Hz to 1/1.4 Hz. The new picks are indicated by vertical dashed lines in Fig. 14.

#### 7.2.2. Core-reflected phases

As described in section 4.2, the computed core-reflected travel time range based on the geodetically-estimated core radius (1700–1900 km) is, for most events, too wide to allow for unambiguous discrimination of the ScS phase. However, predictions based on the preliminary velocity models allow us to reduce the search range significantly. The procedure is illustrated in Fig. 15 for event S0235b. Fig. 15A shows the N-component time-domain envelopes and polarised traces for this event,

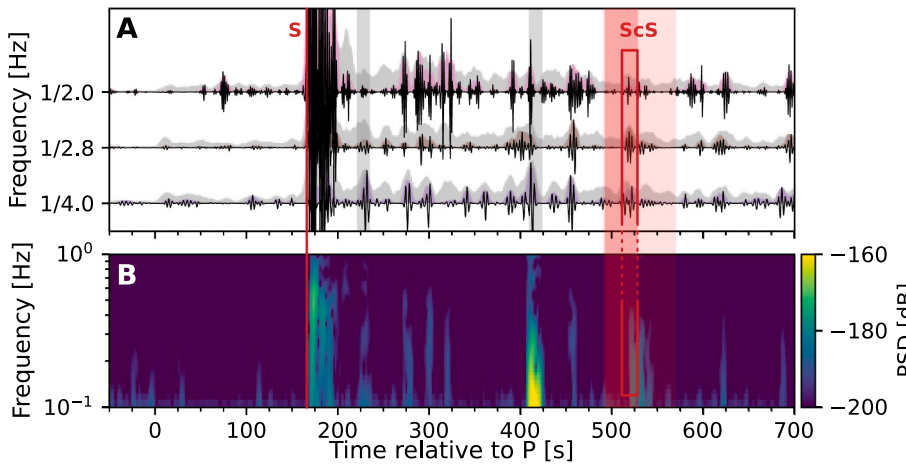


**Fig. 15.** Transverse-component time-domain envelopes and polarised traces across different frequency bands (filter banks) (A) and spectrogram (B) for event S0235b. (A) Time-domain envelopes are shown in grey, while polarised traces and their envelopes are shown in black (lines) and colour, respectively. Vertical grey bars indicate glitches. Amplitudes of traces and envelopes are normalized by their maxima and scaled for better visualisation. The broad light-red vertical bar indicates the predicted arrival time range for ScS based on pre-mission models, while the dark-red vertical bar indicates predicted arrival time range for ScS based on the preliminary velocity models (Fig. 13). The framed red box shows the window in which the ScS arrival is picked. The red vertical line shows the selected S-wave arrival. (For interpretation of the references to colour in this figure legend, the reader is referred to the web version of this article.)

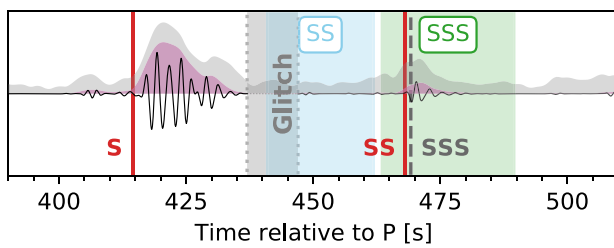


**Fig. 16.** North-component time-domain envelopes and polarised waveforms for event S0167b filtered in a narrow frequency band centered at 1/2 Hz. Vertical bands represent predictions of differential travel times using the inverted preliminary set of velocity models shown in Fig. 13. Vertical solid red lines illustrate the previously selected picks (here S and SS), while the grey dashed line indicates the new arrival based on the predicted differential travel times (here SSS). The grey band between the vertical dotted lines indicates a glitch (denoted ‘Glitch’). (For interpretation of the references to colour in this figure legend, the reader is referred to the web version of this article.)

while Fig. 15B depicts the computed spectrogram. We observe a strong and consistent arrival (indicated by the framed red box) across the filter banks in the range 1/1.4–1/4 Hz that is also clearly visible in the spectrogram.

### 7.2.3. Phase mislabeling

While the use of travel-time predictions based on preliminary inverted models is a useful method for picking additional phases, assigning body-wave arrivals nonetheless depends on the background noise level. Consequently, mislabeling of seismic body-wave arrivals is potentially possible, yet any potential outlier is expected to be identifiable in a subsequent inversion, as it is unlikely to fit the observation. This is illustrated in Fig. 16 for event S0167b, where a strong energy arrival, with a polarisation coincident with the one observed for the S-wave, was initially picked as an SS-wave (solid vertical red line), but the preliminary models suggest that the SS-wave should arrive earlier (blue-shaded area). A glitch is, however, partly present in the horizontal components that coincides with the expected arrival of the SS-wave. Since the selected phase follows the criteria described in section 4.1 and fits the differential travel time predicted for the SSS (green-shaded area), we re-label it as SSS (dashed vertical line).

### 7.2.4. Final data set

Through the application of the abovementioned steps to all events, we are able to iteratively refine and enlarge our data set. We generally attempt to pick phases as consistently as possible using the computed travel-time distributions as guidance, but nonetheless adjust picks where personal judgement deems this necessary. The final refined data set comprising 14 LF events is tabulated in Table 4. Uncertainties on individual arrivals are assigned using the time-domain filter banks and the

**Table 4**

Final set of observed body-wave differential travel times (stage 3). Seismic arrival picks are made based on visual inspection of time-domain envelopes, polarised traces, polarisation analysis, and waveform matching. Source depths are based on inversion of the depth phases (pP and sS) and quoted epicentral distance estimates are obtained from the sampled distributions shown in SM Fig. S24. Depths in italic refer to events for which the depth was fixed to the mean depth based on the observed depth phases. Seismic phases in italic refer to predicted phases that were not used for the inversion. Tabulated times are expressed in seconds after the main P-wave arrival. Absolute P-wave arrival times (UTC) are listed in Table S2. Uncertainties on individual arrivals are assigned using the time-domain filter banks and the polarised traces and typically range between 2 and 8 s for the final set of picks. The events considered here comprise only the highest-quality events. The new seismic data set presented here, including the P-wave arrival time picks listed in Table S2, totals 76 arrival time picks.

Event	T <sub>pP</sub>	T <sub>PP</sub>	T <sub>PPP</sub>	T <sub>S</sub>	T <sub>SS</sub>	T <sub>SS</sub>	T <sub>SSS</sub>	T <sub>PS</sub>	T <sub>ScS</sub>	Depth [km]	Distance [°]
S0167b	–	37.0 ± 3	–	414.5 ± 2	–	–	468.0 ± 3	–	–	31.2	72.5 ± 3.1
S0173a	11.1 ± 3	–	–	174.8 ± 2	184.8 ± 3	197.9 ± 2	–	–	515.0 ± 5	28.7 ± 8.1	30.6 ± 2.8
S0183a	–	24.5 ± 4	43.0 ± 7	–	–	–	–	–	–	31.2	47.9 ± 12.3
S0185a	–	–	–	360.2 ± 2	379.5 ± 4	–	412.5 ± 6	–	–	34.2 ± 8.0	63.1 ± 4.3
S0235b	–	17.4 ± 2	31.1 ± 7	166.0 ± 3	178.7 ± 3	193.1 ± 3	–	168.4 ± 2	512.0 ± 8	27.4 ± 8.3	29.6 ± 1.8
S0325a	11.3 ± 3	–	–	230.7 ± 3	–	260.7 ± 4	281.0 ± 6	–	–	33.1 ± 7.8	42.4 ± 4.3
S0407a	–	17.8 ± 5	33.0 ± 7	172.2 ± 2	183.4 ± 3	196.4 ± 5	–	–	–	32.0 ± 8.5	30.3 ± 3.2
S0409d	–	–	–	162.5 ± 3	–	184.9 ± 4	207.7 ± 6	–	–	31.2	29.8 ± 3.5
S0484b	–	18.1 ± 5	–	170.2 ± 1	184.0 ± 3	196.8 ± 3	–	–	–	33.5 ± 8.0	30.7 ± 4.6
S0784a	–	15.2 ± 4	29.5 ± 7	173.0 ± 4	182.2 ± 4	196.9 ± 5	221.9 ± 6	178.7 ± 2	–	30.6 ± 8.5	31.1 ± 3.1
S0802a	–	17.3 ± 5	–	176.3 ± 5	–	201.5 ± 5	222.1 ± 6	–	–	31.2	31.9 ± 3.6
S0809a	–	15.5 ± 5	29.3 ± 7	175.0 ± 1	–	197.5 ± 3	–	184.0 ± 2	–	31.2	31.3 ± 3.7
S0820a	–	15.7 ± 5	–	176.5 ± 2	186.2 ± 3	201.4 ± 5	–	–	–	30.5 ± 8.2	31.6 ± 4.0
S0864a	–	18.0 ± 5	–	169.0 ± 3	181.2 ± 4	194.0 ± 3	216.1 ± 6	–	505.0 ± 8	31.3 ± 8.1	30.5 ± 3.2

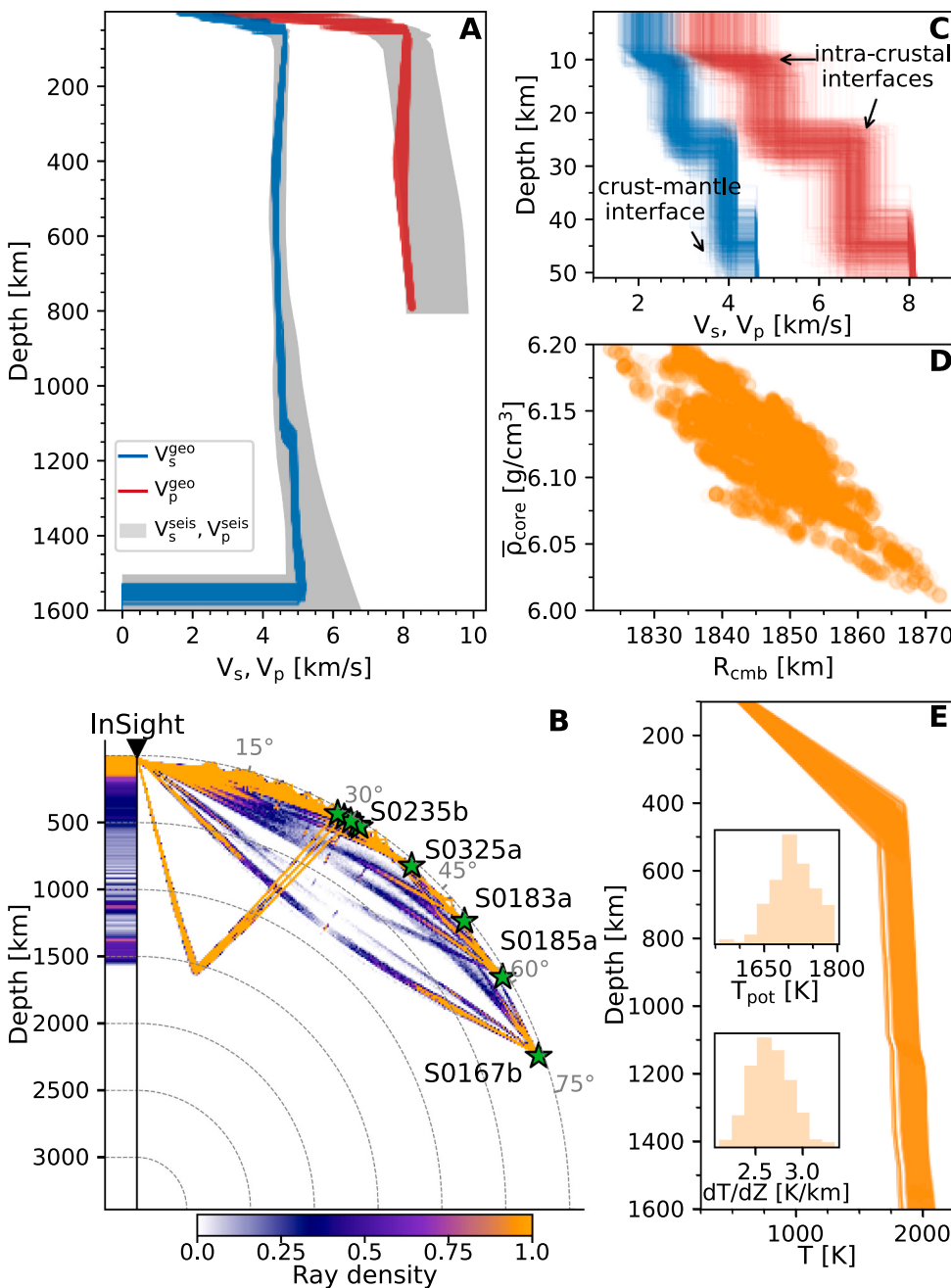


**Fig. 17.** Seismic wave velocity models, ray path geometry, core properties obtained and thermal profiles from inversion of the final set of differential travel times (Table 4). (A) Inverted seismic P- and S-wave velocity profiles based on the geophysical (red and blue) and seismic (grey) parameterisations, respectively. Because there are no observations of P-waves that traverse the lower mantle, P-wave velocity below 800 km depth is not shown. (B) Body-wave (P, S, PP, SS, PPP, SSS, PS, pP, sS, and ScS) ray path geometry for all 14 low-frequency events considered here. The colour bar indicates ray path density, that is, the number of rays that pass through a certain area based on the inverted models shown in (A), which accounts for the diffuseness of ray paths and source locations. The column to the left of “InSight” illustrates the radial sensitivity computed as the integrated ray path density with epicentral distance. For the cluster of events around 30° epicentral distance, only event S0235b is labelled. (C) shows the distributions of sampled crustal P- and S-wave velocity structure. Panel (D) shows inverted mean core density versus core radius. Panel (E) shows the inverted lithospheric and upper mantle geothermal profiles and the insets show the distribution of sampled potential temperature ( $T_{\text{pot}}$ ) and lithospheric geothermal gradients ( $dT/dZ$ ). (For interpretation of the references to colour in this figure legend, the reader is referred to the web version of this article.)

polarised traces and typically range between 2 and 8 s for the additional set of picks.

### 7.3. Stage 3: final inversion

In a final step, we re-invert the entire data set, which includes the stacked RF and the expanded differential travel-time data (Table 4), for a new set of interior structure models and source parameters that are shown in Fig. 17. In Fig. 17A, the inverted P- and S-wave velocity profiles obtained using both the geophysical parameterization (blue and red models) and the seismic parameterization (grey models) are shown. Fig. 17B illustrates the location of events relative to InSight (epicentral distance distributions for all events are shown in supplementary material Fig. S24), and ray path geometry and radial sensitivity for the geophysically-constrained velocity models and the indicated receiver-source configuration. Firstly, we note that the seismic velocity profiles

for both parameterisations are very similar and secondly, that the estimated model parameter ranges in the case of the seismic parameterization are, as expected, wider. The latter observation reflects the fact that the geophysical parameterization incorporates mineral physics information. Thirdly, P-wave velocity is constrained to 800 km depth, because of lack of P-wave observations that sample the deep interior. Fourthly, because we have more S-wave (45) than P-wave (31) observations, P-wave velocity profiles are wider than S-wave velocity profiles.

The results found here are generally in good agreement with earlier published results (Knapmeyer-Endrun et al., 2021; Khan et al., 2021; Stähler et al., 2021). Only a brief discussion will be given here; more detailed analysis will follow elsewhere. Differences between current and earlier results are chiefly due to 1) complete re-analysis of the entire data set, which has resulted in a more robust set of body wave picks; 2) the more-than-significant increase in the number of LF events (14 versus 8) and differential travel-time picks (76 versus 41); and 3) the joint

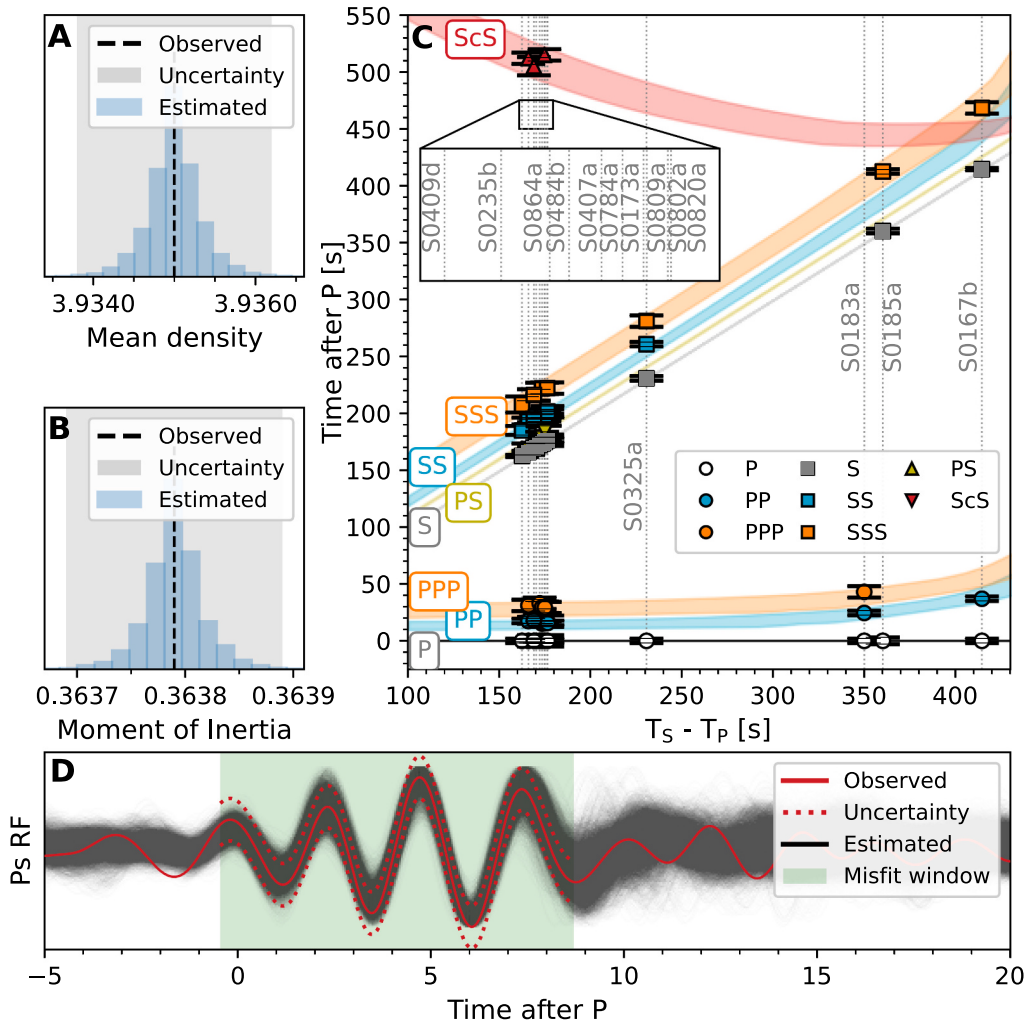


**Fig. 18.** Computed data misfits for mean density (A), moment of inertia (B), differential travel times (C), and converted phases Ps (D) obtained from the final set of inverted models shown in Fig. 17. See main text for details.

inversion of direct, reflected, and converted phases. Relative to the events considered by Khan et al. (2021), we have omitted S0189a because of the difficulty of picking the P-wave arrival based on the present analysis (see supplementary Fig. S25). The P-wave arrival in Khan et al. (2021) was based on the uncertain pick made by MQS. With regard to core-reflections, we have identified fewer ScS arrivals in comparison to Stähler et al. (2021). While Stähler et al. (2021) reported ScS arrivals from 6 events, the arrivals were determined using a set of independent processing methods, resulting in ScS picks with appreciable scatter. This contrasts with the criteria established here, where a seismic phase is required to be compatible with all of our processing schemes to be positively identified.

Figs. 17C and D show zoom-ins of crustal P- and S-wave velocity structure, respectively. We find, as before (Knapmeyer-Endrun et al., 2021; Khan et al., 2021), discontinuities in the depth ranges 8–13 km, 22–27 km, and 37–47 km, respectively, of which the former is most probably an intra-crustal interface and the second or the third (preferred) is likely the Moho. Analysis of other crustal phases appear to support the latter interpretation (e.g., Kim et al. (2021b)). As we model Mars as a spherically symmetric planet, lateral variations in crustal thickness (Wieczorek and Zuber, 2004; Neumann et al., 2004) and possibly in seismic properties (Bozdağ et al., 2017; Bissig et al., 2018) are not studied. While the uncertainty on the main P- and S-wave picks (2–10 s) generally exceed those expected from three-dimensional structure (<3 s) (Bozdağ et al., 2017), and the latter therefore poses

less of a problem, this could be different for the multiply reflected waves. The impact of lateral variations will have to be considered in more detail in the future.

As in our earlier derived models of mantle structure (Khan et al., 2021; Stähler et al., 2021), we also find evidence for an upper mantle low-velocity zone for S-waves. This appears to be a relatively robust feature as it is seen by both parameterisations. In this context, we also predict a slight decrease in P-wave velocity in the upper mantle with depth to 450 km, marking the bottom of the lithosphere (Fig. 17A). The P-wave velocity decrease results from a slightly larger geothermal gradient (Fig. 17E) in the upper mantle (2.4–2.9 K/km; previously 1.6–2.5 K/km). As also indicated in Fig. 17E, we obtain mantle potential temperatures in the range 1650–1750 K, whereas temperatures at the core-mantle-boundary (CMB) reach 1900–2100 K. While the P-wave velocity decrease is only apparent in the profiles obtained from the geophysical parameterisation and is therefore less well-constrained than its S-wave velocity counterpart, an experimental study based on sound velocity measurements on mineralogical assemblages representative of Mars's composition have observed low P- and S-wave velocities at pressures and temperatures equivalent of the upper mantle of Mars (Xu et al., 2021). Continued analysis and not least future events will hopefully fill the current gap in our knowledge of P-wave velocity in the deeper parts of the mantle.

Derived core properties (mean core density and radius) are illustrated in Fig. 17F and indicate a core radius and a mean core density in

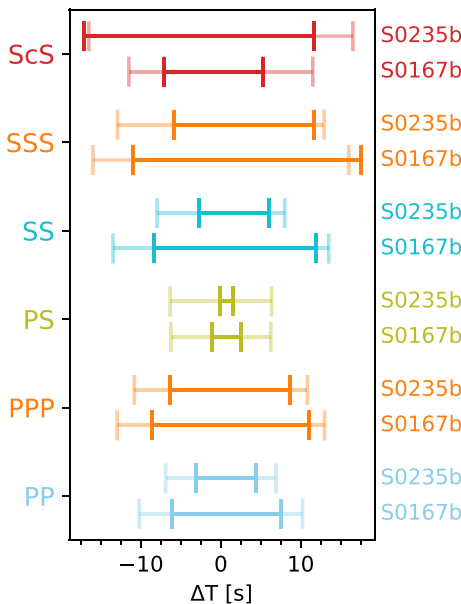


**Fig. 19.** Comparison between differential body-wave travel time predictions based on the preliminary (light colored bands) and final set of models (darker colored bands) for two events (S0167b and S0235b). The gain in information obtained by inverting the final set of picks (Table 4) relative to the initial set of picks (Table 1) is clearly visible.

the ranges 1820–1870 km (previously 1790–1870 km) and 6–6.2 g/cm<sup>3</sup> (previously 5.7–6.3 g/cm<sup>3</sup>), respectively. In agreement with Khan et al. (2022), the core radius range is narrower than determined by Stähler et al. (2021), while the mean core density brackets both a more limited and a higher range relative to what had been determined by Stähler et al. (2021). The narrower range is a consequence of the new mantle compositions estimated by Khan et al. (2022) (Table 2) that are consistent with both geophysical and cosmo- and geochemical data, while the shift to higher mean core densities results from the lower mantle FeO content (<14 wt%) determined by Khan et al. (2022). The mean core density and composition derived here and by Khan et al. (2022), require an appreciable amount of light elements in the core that, when combined with the CMB temperatures found here, are compatible with an entirely liquid core at present.

Finally, data misfits are shown in Fig. 18 and indicate that inverted models fit the observations within uncertainties: mean density (Fig. 18A), mean moment of inertia (Fig. 18B), differential body-wave travel times (Fig. 18C), and RFs (Fig. 18D). To illustrate the gain in information between the initial (*stage 1*) and the final inversion (*stage 3*), we compare differential travel-time misfits for both cases in Fig. 19 for two events. The differential travel-time ranges are, as expected, narrower in the final inversion as a result of the increase in the number of observations between the two stages.

#### 7.4. The mantle transition zone

The upper mantle transition zone (MTZ) in the Earth is delineated by the mineral phase transformation, olivine→wadsleyite, which occurs at an average depth of 410 km (Helffrich, 2000), corresponding to a pressure of ~13 GPa (Ringwood, 1975). The equivalent transition in the mantle of Mars is found to occur at a depth of ~1100–1150 km for the thermo-chemical conditions considered here (see Fig. 17A). As shown in e.g., Munch et al. (2018), the location of the olivine→wadsleyite transition, can be used as a thermometer because it is primarily influenced by temperature conditions in the mantle. Seismic phases sensitive to this transition include body wave conversions at, triplications from, and underside reflections off the MTZ (e.g. Borgeaud et al., 2019; Huang

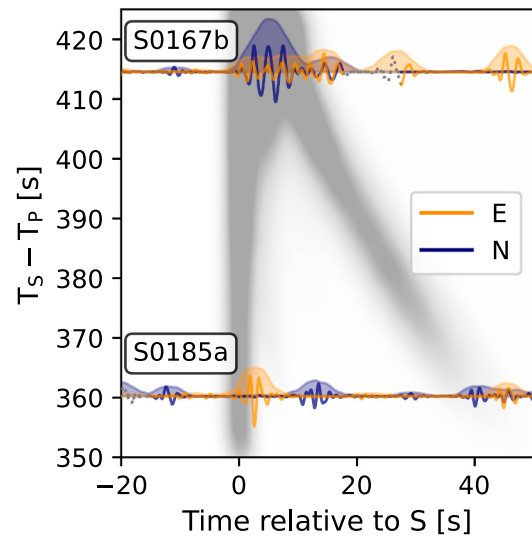


**Fig. 20.** Comparison of differential travel times of triplicated S-waves based on the final set of models (in grey) and the filtered (0.3–0.9 Hz) horizontal-component polarised waveforms of S0167b and S0185a aligned by their respective S-P differential travel time. Dotted sections of the waveforms indicate glitches.

et al., 2019; Bissig et al., 2021). Here we will briefly focus on triplications.

Fig. 20 shows the differential travel-time plot of triplicated S-waves based on our final set of models (in grey) and the filtered (0.3–0.9 Hz) polarised waveforms of S0167b and S0185a aligned by their respective S-P differential travel time that sample the martian MTZ. Event S0185a only intersects the very lower part of the branch and is therefore only weakly sensitive to the MTZ, while S0167b is located in the middle of the triplication. Even though a strong amplitude arrival is observed in the expected range for S0167b, we lack arrivals that sample the triplicated branches either side of S0167b for proper characterisation of the MTZ. Appropriate events could potentially reside among the LF events that have yet to be located. Continued analysis of the data will provide further insight.

#### 8. Conclusions

In this paper, we have described a methodology that determines location (epicentral distance and depth) of Martian seismic events simultaneously with interior structure, while allowing, through iterative refinement, for the identification of additional body-wave arrivals. However, since Martian seismograms are generally characterized by low SNR, show strong scattering, and interference of non-seismic signals, careful data selection and processing is central for the identification and consistent picking of body-wave arrivals. To this end, we employed four complementary approaches consecutively that were applied to each LF event: (1) narrow-band-filtered time-domain envelopes; (2) polarised waveforms and their time-domain envelopes; (3) polarisation analysis; and (4) waveform matching. Methods (1) and (2) are used for picking, whereas (3) and (4) are employed for verification. Through the consistent application of these methods, we are able to identify 76 seismic phases, including the main P- and S-wave arrivals and reflected and converted body-wave arrivals (pP, PP, sS, SS, PPP, SSS, ScS, Ps). This presents a considerable gain in information relative to our earlier analyses that were based on 41 phase arrivals only. Through continued analysis of new events, our knowledge and understanding of the interior of Mars will steadily improve.

## Data availability

Models of interior structure: A set of representative interior structure models derived in this study are available from <https://doi.org/10.18715/IPGP.2022.kzwpiude>.

## CRediT authorship contribution statement

**C. Durán:** Conceptualization, Data curation, Formal analysis, Investigation, Methodology, Software, Visualization, Writing – original draft, Writing – review & editing. **A. Khan:** Conceptualization, Data curation, Formal analysis, Investigation, Methodology, Software, Supervision, Writing – original draft, Writing – review & editing. **S. Ceylan:** Data curation, Formal analysis, Methodology, Software. **G. Zenhäusern:** Visualization, Writing – original draft. **S. Stähler:** Data curation, Writing – review & editing. **J.F. Clinton:** Data curation, Writing – review & editing. **D. Giardini:** Project administration, Supervision, Writing – review & editing.

## Declaration of Competing Interest

None.

## Acknowledgements

We are grateful to two anonymous reviewers for constructive comments. A.C.D., G.Z., and S.C.S. would like to acknowledge support from ETH through the ETH+ funding scheme (ETH+02 19-1: “Planet Mars”). We acknowledge NASA, CNES, partner agencies and institutions (UKSA, SSO, DLR, JPL, IPGP-CNRS, ETHZ, ICL, MPS-MPG), and the operators of JPL, SISMOC, MSDS, IRIS-DMC and PDS for providing SEED SEIS data. The authors declare no competing interests. The InSight event catalog (comprising all events, including phase picks until October 2021) and waveform data are available from the IRIS-DMC, NASA-PDS, SEIS-InSight data portal and IPGP data center ([InSight Mars SEIS Data Service, 2019a](https://doi.org/10.18715/IPGP.2019a), [2019b](https://doi.org/10.18715/IPGP.2019b); [InSight Marsquake Service, 2021](https://doi.org/10.18715/IPGP.2021)). This is InSight contribution 235.

## Appendix A. Supplementary data

Supplementary data to this article, which includes additional figures and tables, can be found online at <https://doi.org/10.1016/j.pepi.2022.106851>.

## References

- Anderson, D.L., Miller, W.F., Latham, G.V., Nakamura, Y., Toksz, M.N., Dainty, A.M., Duennebier, F.K., Lazarewicz, A.R., Kovach, R.L., Knight, T.C.D., 1977. Seismology on Mars. *J. Geophys. Res.* 1896–1977 (82), 4524–4546. <https://doi.org/10.1029/JS082i028p04524>.
- Bagheri, A., Khan, A., Al-Attar, D., Crawford, O., Giardini, D., 2019. Tidal response of Mars constrained from laboratory-based viscoelastic dissipation models and geophysical data. *J. Geophys. Res. Planets* 124, 2703–2727. <https://doi.org/10.1029/2019JE006015>.
- Banerdt, W.B., Smrekar, S.E., Banfield, D., Giardini, D., Golombek, M., Johnson, C.L., Lognonné, P., Spiga, A., Spohn, T., Perrin, C., Stähler, S.C., Antonangeli, D., Asmar, S., Beghein, C., Bowles, N., Bozdag, E., Chi, P., Christensen, U., Clinton, J., Collins, G.S., Daubar, I., Dehant, V., Drilleau, M., Fillingim, M., Folkner, W., Garcia, R.F., Garvin, J., Grant, J., Grott, M., Grygorczuk, J., Hudson, T., Irving, J.C., E., Kargl, G., Kawamura, T., Kedar, S., King, S., Knapmeyer-Endrun, B., Knapmeyer, M., Lemmon, M., Lorenz, R., Maki, J.N., Margerin, L., McLennan, S.M., Michaut, C., Mimoun, D., Mittelholz, A., Mocquet, A., Morgan, P., Mueller, N.T., Murdoch, N., Nagihara, S., Newman, C., Nimmo, F., Panning, M., Pike, W.T., Plesa, A.C., Rodriguez, S., Rodriguez-Manfredi, J.A., Russell, C.T., Schmerr, N., Siegler, M., Stanley, S., Stutzmann, E., Teamby, N., Tromp, J., van Driel, M., Warner, N., Weber, R., Wieczorek, M., 2020. Initial results from the InSight mission on Mars. *Nat. Geosci.* 13, 183–189. <https://doi.org/10.1038/s41561-020-0544-y>.
- Banfield, D., Spiga, A., Newman, C., Forget, F., Lemmon, M., Lorenz, R., Murdoch, N., Viudez-Moreiras, D., Pla-Garcia, J., Garcia, R.F., et al., 2020. The atmosphere of Mars as observed by InSight. *Nat. Geosci.* 13, 190–198.
- Bissig, F., Khan, A., van Driel, M., Stähler, S.C., Giardini, D., Panning, M., Drilleau, M., Lognonné, P., Gudkova, T.V., Zharkov, V.N., Plesa, A.C., Banerdt, W.B., 2018. On the detectability and use of Normal modes for determining interior structure of Mars. *Space Sci. Rev.* 214, 114. <https://doi.org/10.1007/s11214-018-0547-9>.
- Bissig, F., Khan, A., Tauzin, B., Sossi, P.A., Munch, F.D., Giardini, D., 2021. Multifrequency inversion of Ps and Sp receiver functions: methodology and application to USArray data. *Journal of geophysical research: solid Earth* 126, e2020JB020350. <https://doi.org/10.1029/2020JB020350> e2020JB020350.
- Borgeaud, A.F.E., Kawai, K., Geller, R.J., 2019. Three-dimensional S velocity structure of the mantle transition zone beneath Central America and the Gulf of Mexico inferred using waveform inversion. *J. Geophys. Res. Solid Earth* 124, 9664–9681. <https://doi.org/10.1029/2018JB016924>.
- Böse, M., Clinton, J.F., Ceylan, S., Euchner, F., van Driel, M., Khan, A., Giardini, D., Lognonné, P., Banerdt, W.B., 2017. A probabilistic framework for single-station location of seismicity on earth and Mars. *Phys. Earth Planet. Inter.* 262, 48–65.
- Böse, M., Giardini, D., Stähler, S., Ceylan, S., Clinton, J.F., van Driel, M., Khan, A., Euchner, F., Lognonné, P., Banerdt, W.B., 2018. Magnitude scales for marsquakes. *Bull. Seismol. Soc. Am.* 108, 2764–2777.
- Böse, M., Horleston, A.C., Stähler, S.C., Deichmann, D., Giardini, D., Clinton, J., Lognonné, P., Ceylan, S., van Driel, M., Charalambous, C., et al., 2021. Magnitude scales for Marsquakes calibrated from InSight data. *Bull. Seismol. Soc. Am.* 111 (6), 3003–3015.
- Bozdağ, E., Ruan, Y., Metthez, N., Khan, A., Leng, K., van Driel, M., Wieczorek, M., Rivoldini, A., Larmat, C.S., Giardini, D., Tromp, J., Lognonné, P., Banerdt, B.W., 2017. Simulations of seismic wave propagation on Mars. *Space Sci. Rev.* 211, 571–594. <https://doi.org/10.1007/s11214-017-0350-z>.
- Ceylan, S., Clinton, J.F., Giardini, D., Böse, M., Charalambous, C., van Driel, M., Horleston, A., Kawamura, T., Khan, A., Orhand-Mainsant, G., et al., 2021. Companion guide to the marsquake catalog from InSight, sols 0–478: data content and non-seismic events. *Phys. Earth Planet. Inter.* 310, 106597.
- Choy, G.L., Richards, P.G., 1975. Pulse distortion and Hilbert transformation in multiply reflected and refracted body waves. *Bull. Seismol. Soc. Am.* 65, 55–70.
- Clinton, J.F., Giardini, D., Lognonné, P., Banerdt, B., van Driel, M., Drilleau, M., Murdoch, N., Panning, M., Garcia, R., Mimoun, D., et al., 2017. Preparing for InSight: an invitation to participate in a blind test for Martian seismicity. *Seismol. Res. Lett.* 88, 1290–1302.
- Clinton, J.F., Ceylan, S., van Driel, M., Giardini, D., Stähler, S.C., Böse, M., Charalambous, C., Dahmen, N.J., Horleston, A., Kawamura, T., Khan, A., Orhand-Mainsant, G., Scholz, J.R., Euchner, F., Banerdt, B.W., Lognonné, P., Banerdt, D., Beucler, E., Garcia, R.F., Kedar, S., Panning, M.P., Perrin, C., Pike, W.T., Smrekar, S.E., Spiga, A., Stott, A.E., 2021. The Marsquake catalogue from InSight, sols 0–478. *Phys. Earth Planet. Inter.* 310, 106595. <https://doi.org/10.1016/j.pepi.2020.106595>.
- Connolly, J.A.D., 2009. The geodynamic equation of state: what and how. *Geochem. Geophys. Geosyst.* 10, Q10014. <https://doi.org/10.1029/2009GC002540>.
- Crotwell, H.P., Owens, T.J., Ritsema, J., 1999. The TauP toolkit: flexible seismic travel-time and ray-path Utilities. *Seismol. Res. Lett.* 70, 154–160. <https://doi.org/10.1785/gssr.70.2.154>.
- Dahmen, N.L., Clinton, J.F., Ceylan, S., van Driel, M., Giardini, D., Khan, A., Stähler, S.C., Böse, M., Charalambous, C., Horleston, A., et al., 2021. Super high frequency events: a new class of events recorded by the InSight seismometers on Mars. *J. Geophys. Res.* 126 e2020JE006599.
- van Driel, M., Ceylan, S., Clinton, J.F., Giardini, D., Horleston, A., Margerin, L., Stähler, S.C., Böse, M., Charalambous, C., Kawamura, T., et al., 2021. High-frequency seismic events on Mars observed by InSight. *J. Geophys. Res.* 126 e2020JE006670.
- Drilleau, M., Beucler, R., Lognonné, P., Panning, M.P., Knapmeyer-Endrun, B., Banerdt, W.B., Beghein, C., Ceylan, S., van Driel, M., Joshi, R., Kawamura, T., Khan, A., Menina, S., Rivoldini, A., Samuel, H., Sthler, S., Xu, H., Bonni, M., Clinton, J., Giardini, D., Kenda, B., Lekic, V., Mocquet, A., Murdoch, N., Schimmel, M., Smrekar, S.E., Stutzmann, L., Tauzin, B., Tharimena, S., 2020. MSS/1: single-station and single-event marsquake inversion. *Earth Space Sci.* 7 <https://doi.org/10.1029/2020EA001118> e2020EA001118.
- Fuchs, K., Müller, G., 1971. Computation of synthetic seismograms with the reflectivity method and comparison with observations. *Geophys. J. Int.* 23, 417–433.
- Garcia, R.F., Khan, A., Drilleau, M., Margerin, L., Kawamura, T., Sun, D., Wieczorek, M.A., Rivoldini, A., Nunn, C., Weber, R.C., Marusik, A.G., Lognonné, P., Nakamura, Y., Zhu, P., 2019. Lunar seismology: an update on interior structure models. *Space Sci. Rev.* 215, 50. <https://doi.org/10.1007/s11214-019-0613-y>.
- Giardini, D., Lognonné, P., Banerdt, W.B., Pike, W.T., Christensen, U., Ceylan, S., Clinton, J.F., van Driel, M., Stähler, S., Böse, M., Garcia, R.F., Khan, A., Panning, M., Perrin, C., Banfield, D., Beucler, E., Charalambous, C., Euchner, F., Horleston, A., Jacob, A., Kawamura, T., Kedar, S., Orhand-Mainsant, G., Scholz, J.R., Smrekar, S., Spiga, A., Agard, C., Antonangeli, D., Barksouli, S., Barrett, E., Combès, P., Conejero, V., Daubar, I., Drilleau, M., Ferrier, C., Gabsi, T., Gudkova, T., Hurst, K., Karakostas, F., King, S., Knapmeyer, M., Knapmeyer-Endrun, B., Llorca-Cejudo, R., Lucas, A., Luno, L., Margerin, L., McClean, J., Mimoun, D., Murdoch, N., Nimmo, F., Nonon, M., Pardo, C., Rivoldini, A., Rodriguez Manfredi, J.A., Samuel, H., Schimmel, M., Stott, A.E., Stutzman, E., Teamby, N., Warren, T., Weber, R., Wieczorek, M., Yana, C., 2020. The seismicity of Mars. *Nat. Geosci.* 13, 205–212. <https://doi.org/10.1038/s41561-020-0539-8>.
- Haubrich, R., Munk, W., Snodgrass, F., 1963. Comparative spectra of microseisms and swell. *Bull. Seismol. Soc. Am.* 53, 27–37.
- Helffrich, G., 2000. Topography of the transition zone discontinuities. *Rev. Geophys.* 38, 141–158. <https://doi.org/10.1029/1999RG000060>.
- Hobiger, M., Hallo, M., Schmelzbach, C., Stähler, S., Fäh, D., Giardini, D., Golombek, M., Clinton, J., Dahmen, N., Zenhäusern, G., et al., 2021. The shallow structure of Mars at the InSight landing site from inversion of ambient vibrations. *Nat. Commun.* 12, 6756. <https://doi.org/10.1038/s41467-021-26957-7>.

- Huang, Q., Schmerr, N., Waszek, L., Beghein, C., 2019. Constraints on seismic anisotropy in the mantle transition zone from long-period ss precursors. *J. Geophys. Res. Solid Earth* 124, 6779–6800. <https://doi.org/10.1029/2019JB017307>.
- InSight Mars SEIS Data Service, 2019a. InSight SEIS Data Bundle. PDS Geosciences (GEO) Node. <https://doi.org/10.17189/1517570>.
- InSight Mars SEIS Data Service, 2019b. SEIS Raw Data, Insight Mission. IPGP, JPL, CNES, ETHZ, ICL, MPS, ISAE-Supaero, LPG, MFSC. <https://doi.org/10.18715/SEIS.INSIGHT.XB/a/2016>.
- InSight Marsquake Service, 2021. Mars Seismic Catalogue, Insight Mission; v8 2021-10-01. <https://doi.org/10.12686/a13>.
- Jeffreys, H., Lawood, E., 1957. The reflexion of a pulse within a sphere. *Proc. R. Soc. Lond. Ser. A* 241, 455–479.
- Khan, A., Mosegaard, K., 2002. An inquiry into the lunar interior: a nonlinear inversion of the Apollo lunar seismic data. *J. Geophys. Res. Planets* 107. <https://doi.org/10.1029/2001JE001658>, 3–13–23.
- Khan, A., Pommier, A., Neumann, G., Mosegaard, K., 2013. The lunar moho and the internal structure of the Moon: a geophysical perspective. *Tectonophysics* 609, 331–352. <https://doi.org/10.1016/j.tecto.2013.02.024>.
- Khan, A., van Driel, M., Böse, M., Giardini, D., Ceylan, S., Yan, J., Clinton, J., Euchner, F., Lognonné, P., Murdoch, N., Mimoun, D., Panning, M., Knapmeyer, M., Banerdt, W. B., 2016. Single-station and single-event marsquake location and inversion for structure using synthetic Martian waveforms. *Phys. Earth Planet. Inter.* 258, 28–42. <https://doi.org/10.1016/j.pepi.2016.05.017>.
- Khan, A., Liebske, C., Rozel, A., Rivoldini, A., Nimmo, F., Connolly, J.A.D., Plesa, A.C., Giardini, D., 2018. A geophysical perspective on the bulk composition of Mars. *J. Geophys. Res. Planets* 123, 575–611. <https://doi.org/10.1002/2017JE005371>.
- Khan, A., Ceylan, S., van Driel, M., Giardini, D., Lognonné, P., Samuel, H., Schmerr, N.C., Stähler, S.C., Duran, A.C., Huang, Q., Kim, D., Broquet, A., Charalambous, C., Clinton, J.F., Davis, P.M., Drilleau, M., Karakostas, F., Lekic, V., McLennan, S.M., Maguire, R.R., Michaut, C., Panning, M.P., Pike, W.T., Pinot, B., Plasman, M., Scholz, J.R., Widmer-Schnidrig, R., Spohn, T., Smrekar, S.E., Banerdt, W.B., 2021. Upper mantle structure of Mars from InSight seismic data. *Science* 373, 434–438. <https://doi.org/10.1126/science.abf2966>.
- Khan, A., Sossi, P., Liebske, C., Rivoldini, A., Giardini, D., 2022. Geophysical and cosmochemical evidence for a volatile-rich Mars. *Earth Planet. Sci. Lett.* 578, 117330. <https://doi.org/10.1016/j.epsl.2021.117330>.
- Kim, D., Davis, P., Leki, V., Maguire, R., Compaire, N., Schimmel, M., Stutzmann, E., Irving, C.E., Lognonné, P., Scholz, J., Clinton, J., Zehnhausen, G., Dahmen, N., Deng, S., Levander, A., Panning, M.P., Garcia, R.F., Giardini, D., Hurst, K., Knapmeyer-Endrun, B., Nimmo, F., Pike, W.T., Pou, L., Schmerr, N., Stähler, S.C., Tauzin, B., Widmer-Schnidrig, R., Banerdt, W.B., 2021a. Potential pitfalls in the analysis and structural interpretation of seismic data from the mars insight mission. *Bull. Seismol. Soc. Am.* <https://doi.org/10.1785/0120210123>.
- Kim, D., Leki, V., Irving, J., Schmerr, N., Knapmeyer-Endrun, B., Joshi, R., Panning, M., Tauzin, B., Karakostas, F., Maguire, R., Huang, Q., Ceylan, S., Khan, A., Giardini, D., Wiegczorek, M.A., Lognonné, P., Banerdt, W.B., 2021b. Improving constraints on planetary interiors with pps receiver functions. *J. Geophys. Res.* e2021JE006983. <https://doi.org/10.1029/2021JE006983>.
- King, R., Yuan, X., Kumar, P., 2012. Seismic receiver functions and the lithosphere–asthenosphere boundary. *Tectonophysics* 536, 25–43.
- Knapmeyer-Endrun, B., Panning, M.P., Bissig, F., Joshi, R., Khan, A., Kim, D., Lekić, V., Tauzin, B., Tharimena, S., Plasman, M., Compaire, N., Garcia, R.F., Margerin, L., Schimmel, M., Stutzmann, E., Schmerr, N., Bozdag, E., Plesa, A.C., Wiegczorek, M.A., Broquet, A., Antonangeli, D., McLennan, S.M., Samuel, H., Michaut, C., Pan, L., Smrekar, S.E., Johnson, C.L., Brinkman, N., Mittelholz, A., Rivoldini, A., Davis, P.M., Lognonné, P., Pinot, B., Scholz, J.R., Stähler, S., Knapmeyer, M., van Driel, M., Giardini, D., Banerdt, W.B., 2021. Thickness and structure of the martian crust from InSight seismic data. *Science* 373, 438–443. <https://doi.org/10.1126/science.abf8966>.
- Konopliv, A.S., Park, R.S., Rivoldini, A., Baland, R.M., Le Maistre, S., Van Hoolst, T., Yseboodt, M., Dehant, V., 2020. Detection of the Chandler wobble of Mars from orbiting spacecraft. *Geophys. Res. Lett.* 47 e2020GL090568.
- Kristeková, M., Kristek, J., Moczo, P., 2009. Time-frequency misfit and goodness-of-fit criteria for quantitative comparison of time signals. *Geophys. J. Int.* 178, 813–825.
- Ksanfomality, L.V., Zubkova, V.M., Morozov, N.A., Petrova, E.V., 1982. Microseisms at the VENERA-13 and VENERA-14 landing sites. *Sov. Astron. Lett.* 8, 241.
- Langston, C.A., 1979. Structure under Mount Rainier, Washington, inferred from teleseismic body waves. *J. Geophys. Res. Solid Earth* 84, 4749–4762.
- Latham, G.V., Ewing, M., Press, F., Sutton, G., Dorman, J., Nakamura, Y., Toksz, N., Wiggins, R., Derr, J., Duennebier, F., 1970. Passive seismic experiment. *Science* 167, 455–457.
- Ligorri, J.P., Ammon, C.J., 1999. Iterative deconvolution and receiver-function estimation. *Bull. Seismol. Soc. Am.* 89, 1395–1400.
- Lognonné, P., Johnson, C., 2007. 10.03 - planetary seismology. In: Schubert, G. (Ed.), *Treatise on Geophysics*. Elsevier, Amsterdam, pp. 69–122. <https://doi.org/10.1016/B978-044452748-6.00154-1>.
- Lognonné, P., Banerdt, W.B., Giardini, D., Pike, W., Christensen, U., Lauden, P., de Raucourt, S., Zweifel, P., Calcutt, S., Bierwirth, M., Hurst, K., Ijpeelaan, F., Umland, J., Llorca-Cejudo, R., Larson, S., Garcia, R., Kedar, S., Knapmeyer-Endrun, B., Mimoun, D., Mocquet, A., Panning, M., Weber, R., Sylvester-Baron, A., Pont, G., Verdier, N., Kerjean, L., Facto, L., Gharakhanian, V., Feldman, J., Hoffman, T., Klein, D.B., Klein, K., Onufre, N., Paredes-Garcia, J., Petkov, M., Willis, J., Smrekar, S., Drilleau, M., Gabsi, T., Nebut, T., Robert, O., Tillier, S., Moreau, C., Parise, M., Aveni, G., Ben Charef, S., Bennour, Y., Camus, T., Dandonneau, P., Desfoux, C., Lecomte, B., Pot, O., Revuz, P., Mance, D., ten Pierick, J., Bowles, N., Charalambous, C., Delahunty, A., Hurley, J., Irshad, R., Liu, H., Mukherjee, A., Standley, I., Stott, A., Temple, J., Warren, T., Eberhardt, M., Kramer, A., Kühne, W., Miettinen, E.P., Monecke, M., Aicardi, C., André, M., Baroukh, J., Borrien, A., Bouisset, A., Boutte, P., Brethomé, K., Brysbaert, C., Carlier, T., Deleuze, M., Desmarres, J.M., Dilhan, D., Doucet, C., Faye, D., Faye-Refalo, N., Gonzalez, R., Imbert, C., Larigauderie, C., Locatelli, E., Luno, L., Meyer, J. R., Mialhe, F., Mouret, J.M., Nonon, M., Pahn, Y., Paillet, A., Pasquier, P., Perez, G., Perez, R., Perrin, L., Pouilloux, B., Rosak, A., Savin de Larclause, I., Sicre, J., Sodki, M., Toulemon, N., Vella, B., Yana, C., Alibay, F., Avals, O., Balzer, M., Bhandari, P., Blanco, E., Bone, B., Bousman, J., Bruneau, P., Calef, F., Calvet, R., D'Agostino, S., de los Santos, G., Deen, R., Denise, R., Ervin, J., Ferraro, N., Gengi, H., Grinblat, F., Hernandez, D., Hetzel, M., Johnson, M.E., Khachikyan, L., Lin, J., Madzunkov, S., Marshall, S., Mikellides, I., Miller, E., Raff, W., Singer, J., Sunday, C., Villavazo, J., Wallace, M., Banfield, D., Rodriguez-Manfredi, J., Russell, C., Trebi-Ollennu, A., Maki, J., Beucler, E., Böse, M., Bonjour, C., Berenguer, J., Ceylan, S., Clinton, J., Conejero, V., Daubar, I., Dehant, V., Delage, P., Euchner, H., Estève, I., Fayon, L., Ferriolli, L., Johnson, C.L., Gagnepain-Beyneix, J., Golombek, M., Khan, A., Kawamura, T., Kenda, B., Labrot, P., Murdoch, N., Pardo, C., Perrin, C., Pou, L., Sauron, A., Savoie, D., Stähler, S., Stutzmann, E., Teanby, N., Tromp, J., van Driel, M., Wiegczorek, M., Widmer-Schnidrig, R., Wooley, J., 2019. SEIS: insight's seismic experiment for internal structure of Mars. *Space Sci. Rev.* 215, 12. <https://doi.org/10.1007/s11214-018-0574-6>.
- Lognonné, P., Banerdt, W., Pike, W., Giardini, D., Christensen, U., Garcia, R., Kawamura, T., Kedar, S., Knapmeyer-Endrun, B., Margerin, L., Nimmo, F., Panning, M., Tauzin, B., Scholz, J.R., Antonangeli, D., Barkaoui, S., Beucler, E., Bissig, F., Brinkman, N., Calvet, M., Ceylan, S., Charalambous, C., Davis, P., van Driel, M., Drilleau, M., Fayon, L., Joshi, R., Kenda, B., Khan, A., Knapmeyer, M., Lekic, V., McClean, J., Mimoun, D., Murdoch, N., Pan, L., Perrin, C., Pinot, B., Pou, L., Menina, S., Rodriguez, S., Schmelzbach, C., Schmerr, N., Sollberger, D., Spiga, A., Stähler, S., Stott, A., Stutzmann, E., Tharimena, S., Widmer-Schnidrig, R., Andersson, F., Ansan, V., Beghein, C., Böse, M., Bozdag, E., Clinton, J., Daubar, I., Delage, P., Fuji, N., Golombok, M., Grott, M., Horleston, A., Hurst, K., Irving, J., Jacob, A., Knollenberg, J., Krasner, S., Krause, C., Lorenz, R., Michaut, C., Myhill, B., Nissen-Meyer, T., ten Pierick, J., Plesa, A.C., Quantin-Nataf, C., Robertson, J., Rochas, L., Schimmel, M., Smrekar, S., Spohn, T., Teanby, N., Tromp, J., Vallade, J., Verdier, N., Vrettos, C., Weber, R., Banfield, D., Barrett, E., Bierwirth, E., Calcutt, S., Compaire, N., Johnson, C., Mance, D., Euchner, F., Kerjean, L., Mainsant, G., Mocquet, A., Antonio Rodriguez Manfredi, J., Pont, G., Laudet, P., Nebut, T., de Raucourt, S., Robert, O., Russell, C., Sylvester-Baron, A., Tillier, S., Warren, T., Wiegczorek, M., Yana, C., Zweifel, P., 2020. Constraints on the shallow elastic and anelastic structure of Mars from InSight seismic data. *Nat. Geosci.* 13, 213–220. <https://doi.org/10.1038/s41561-020-0536-y>.
- Montalbetti, J.F., Kanasewich, E.R., 1970. Enhancement of Teleseismic body phases with a polarization filter. *Geophys. J. Int.* 21, 119–129. <https://doi.org/10.1111/j.1365-246X.1970.tb01771.x>.
- Mosegaard, K., Tarantola, A., 1995. Monte Carlo sampling of solutions to inverse problems. *J. Geophys. Res. Solid Earth* 100, 12431–12447.
- Müller, G., 1985. The reflectivity method: a tutorial. *J. Geophys.* 58, 153–174.
- Munch, F.D., Khan, A., Tauzin, B., Zunino, A., Giardini, D., 2018. Stochastic inversion of P-to-S converted waves for mantle composition and thermal structure: methodology and application. *J. Geophys. Res. Solid Earth* 123, 31–51.
- Nakamura, Y., 1983. Seismic velocity structure of the lunar mantle. *J. Geophys. Res. Solid Earth* 88, 677–686.
- Neumann, G.A., Zuber, M.T., Wiegczorek, M.A., McGovern, P.J., Lemoine, F.G., Smith, D. E., 2004. Crustal structure of Mars from gravity and topography. *J. Geophys. Res. Planets* 109, E08002. <https://doi.org/10.1029/2004JE002262>.
- Panning, M.P., Beucler, É., Drilleau, M., Mocquet, A., Lognonné, P., Banerdt, W.B., 2015. Verifying single-station seismic approaches using earth-based data: preparation for data return from the InSight mission to Mars. *Icarus* 248, 230–242. <https://doi.org/10.1016/j.icarus.2014.10.035>.
- Ringwood, A.E., 1975. Composition and Petrology of the Earth's Mantle. McGraw-Hill, New York.
- Rivoldini, A., Van Hoolst, T., Verhoeven, O., Mocquet, A., Dehant, V., 2011. Geodesy constraints on the interior structure and composition of Mars. *Icarus* 213, 451–472. <https://doi.org/10.1016/j.icarus.2011.03.024>.
- Rondenay, S., 2009. Upper mantle imaging with array recordings of converted and scattered teleseismic waves. *Surv. Geophys.* 30, 377–405.
- Samson, J., 1983. Pure states, polarized waves, and principal components in the spectra of multiple, geophysical time-series. *Geophys. J. Int.* 72, 647–664.
- Schimmel, M., Gallart, J., 2003. The use of instantaneous polarization attributes for seismic signal detection and image enhancement. *Geophys. J. Int.* 155, 653–668.
- Schimmel, M., Stutzmann, E., Arduhin, F., Gallart, J., 2011. Polarized earth's ambient microseismic noise. *Geochem. Geophys. Geosyst.* 12.
- Scholz, J.R., Widmer-Schnidrig, R., Davis, P., Lognonné, P., Pinot, B., Garcia, R.F., Hurst, K., Pou, L., Nimmo, F., Barkaoui, S., de Raucourt, S., Knapmeyer-Endrun, B., Knapmeyer, M., Mainsant, G., Compaire, N., Cuvier, A., Beucler, R., Bonnin, M., Joshi, R., Sainton, G., Stutzmann, E., Schimmel, M., Horleston, A., Bse, M., Ceylan, S., Clinton, J., van Driel, M., Kawamura, T., Khan, A., Stähler, S.C., Giardini, D., Charalambous, C., Stott, A.E., Pike, W.T., Christensen, U.R., Banerdt, W. B., 2020. Detection, analysis and removal of glitches from InSights seismic data from Mars. *Earth Space Sci.* 7 <https://doi.org/10.1029/2020EA001317-T>.
- Smrekar, S.E., Lognonné, P., Spohn, T., Banerdt, W.B., Breuer, D., Christensen, U., Dehant, V., Drilleau, M., Folkner, W., Fuji, N., et al., 2019. Pre-mission insights on the interior of mars. *Space Sci. Rev.* 215, 3.
- Stähler, S.C., Khan, A., Banerdt, W.B., Lognonné, P., Giardini, D., Ceylan, S., Drilleau, M., Duran, A.C., Garcia, R.F., Huang, Q., Kim, D., Lekic, V., Samuel, H., Schimmel, M.,

- Schmerr, N., Sollberger, D., Stutzmann, É., Xu, Z., Antonangeli, D., Charalambous, C., Davis, P.M., Irving, J.C.E., Kawamura, T., Knapmeyer, M., Maguire, R., Marusiak, A.G., Panning, M.P., Perrin, C., Plesa, A.C., Rivoldini, A., Schmelzbach, C., Zenhäusern, G., Beucler, É., Clinton, J., Dahmen, N., van Driel, M., Gudkova, T., Horleston, A., Pike, W.T., Plasman, M., Smrekar, S.E., 2021. Seismic detection of the martian core. *Science* 373, 443–448. <https://doi.org/10.1126/science.abi7730>.
- Stixrude, L., Lithgow-Bertelloni, C., 2005. Thermodynamics of mantle minerals – I. Physical properties. *Geophys. J. Int.* 162, 610–632. <https://doi.org/10.1111/j.1365-246X.2005.02642.x>.
- Stixrude, L., Lithgow-Bertelloni, C., 2011. Thermodynamics of mantle minerals – II. Phase equilibria. *Geophys. J. Int.* 184, 1180–1213. <https://doi.org/10.1111/j.1365-246X.2010.04890.x>.
- Tanimoto, T., Ishimaru, S., Alvizuri, C., 2006. Seasonality in particle motion of microseisms. *Geophys. J. Int.* 166, 253–266.
- Vinnik, L., 1977. Detection of waves converted from P to SV in the mantle. *Phys. Earth Planet. Inter.* 15, 39–45.
- Weber, R.C., Lin, P.Y., Garnero, E.J., Williams, Q., Lognonné, P., 2011. Seismic detection of the lunar core. *Science* 331, 309–312. <https://doi.org/10.1126/science.1199375>.
- Wieczorek, M.A., Zuber, M.T., 2004. Thickness of the Martian crust: improved constraints from geoid-to-topography ratios. *J. Geophys. Res. Planets* 109, E01009. <https://doi.org/10.1029/2003JE002153>.
- Xu, F., Siersch, N.C., Graux, S., Rivoldini, A., Kuwahara, H., Kondo, N., Wehr, N., Menguy, N., Kono, Y., Higo, Y., Plesa, A.C., Badro, J., Antonangeli, D., 2021. Low velocity zones in the Martian upper mantle highlighted by sound velocity measurements. *Geophys. Res. Lett.* e2021GL093977 <https://doi.org/10.1029/2021GL093977>.